

Real-Time Fault-Tolerant Moving Horizon Air Data Estimation for the RECONFIGURE benchmark

Yiming Wan and Tamás Keviczky

Abstract—This paper proposes a real-time fault-tolerant estimation approach for combined sensor fault diagnosis and air data reconstruction. Due to simultaneous influence of winds and latent faults on monitored sensors, it is challenging to address the trade-off between robustness to wind disturbances and sensitivity to sensor faults. As opposed to conventional fault-tolerant estimators that do not consider any constraints, we propose a constrained fault-tolerant estimator using moving horizon estimation. By exploiting wind bounds according to the weather or flight conditions, this approach improves fault sensitivity without sacrificing disturbance robustness. This improvement is attributed to active inequality constraints caused by faults, as shown in sensitivity analysis of the formulated moving horizon estimation problem. The challenge of real-time nonlinear moving horizon estimation is addressed by adopting an efficient structure-exploiting algorithm within a real-time iteration scheme. In order to facilitate the industrial validation and verification, the algorithm is implemented using an Airbus graphical symbol library to be compliant with the actual flight control computer, and its feasibility of real-time computation has been validated. The simulation results on the RECONFIGURE benchmark, which is a high-fidelity Airbus simulator, over a wide range of the flight envelope show the efficacy of the proposed approach.

Index Terms—Fault detection and isolation, moving horizon estimation, real-time computation, aerospace.

I. INTRODUCTION

DURING aircraft operations, air data measurements are fed into the flight control computer (FCC) to calculate the flight control law, thus it is critical to ensure availability and reliability of air data measurements [1]. The industrial state-of-the-art for civil aircraft relies on triplex hardware redundancy, and performs a majority voting scheme to select the reliable measurements and discard any failed sources [1]. This scheme works well if only one sensor source becomes faulty, but it is inadequate to address simultaneous multiple sensor faults within the triplex redundancy. As recently investigated in the RECONFIGURE project [1], one possibility to extend guidance and control functionalities without adding additional redundant sensors could be the incorporation of analytical redundancy to (i) detect and isolate sensor faults, and (ii) provide reliable air data estimation.

This work has received funding from the European Union’s Seventh Framework Programme (FP7-RECONFIGURE/2007-2013) under grant agreement no. 314544.

Yiming Wan is with School of Automation, Huazhong University of Science and Technology, Wuhan, China and with Massachusetts Institute of Technology, Cambridge, MA 02139, USA. Email: ywan@mit.edu

Tamás Keviczky is with the Delft Center for Systems and Control, Delft University of Technology, 2628 CD, Delft, The Netherlands. Email: t.keviczky@tudelft.nl

Reliable state/parameter estimation in the presence of faults highly relies on accurate and prompt fault detection and isolation (FDI). The combination of these two tasks is referred to as fault-tolerant estimation (FTE) in some literature, e.g., the multiple-model approach in [2]–[4], the adaptive Kalman filtering approach in [5], [6], and the moving horizon estimation approach exploiting a sparsity constraint on faults in [7]. FTE is also an important part in a fault-tolerant control system [8], [9]. Depending on the type of adopted models, existing FDI and estimation approaches for aircraft sensors can be classified into two categories. The first category uses an aerodynamics-dependent model, e.g., [10]–[15]. The FDI and estimation methods for such a model need to explicitly address the robustness against uncertain aerodynamics. Moreover, the aerodynamic coefficients highly depend on the specific aircraft structure and flight envelope, thus the corresponding FDI and estimation methods might fail in any unexpected condition [16]. In contrast, the second category adopts an aerodynamics-independent model, e.g., the wind velocity triangle [17]–[19], the aircraft dynamic model with three-axis load factors as inputs [20]–[22], or a combination of the above two models [16], [23]. Such aerodynamics-independent models simplify the design of FDI and estimation algorithms by avoiding the use of uncertain aerodynamics, hence the corresponding algorithms can be easily configured for different aircraft without adapting to the changing aerodynamics [16], [20].

To achieve air data estimation tolerant to sensor faults, a crucial issue is to distinguish wind disturbances from faults in FDI [24]. With the assumption of constant winds, an extended Kalman filter (EKF) was developed in [17]–[19] to estimate both winds and the airspeed calibration factor by utilizing the wind velocity triangle. The limitation of this approach is that the estimation performance is highly affected by the fulfilment of the persistence of excitation condition which is not satisfied in some aircraft maneuvers [18], [19]. In [20], it was shown that the airspeed-based kinematic model is not affected under constant winds. Moreover, the groundspeed-based kinematic model is insensitive to time-varying winds, and it was used in [21] to address the inertial measurement unit sensor fault reconstruction problem by an adaptive two-stage EKF. For an aerodynamics-dependent model subject to winds, the disturbance decoupling method based on differential geometry was adopted in [10] to perfectly decouple the wind effect in the generated residual signal. In [25], another aerodynamic-dependent Takagi-Sugeno fuzzy model was established to represent the nonlinear dynamics without considering the wind effect, and a bank of sliding mode observers were designed for sensor fault diagnosis and estimation.

In contrast to the above literature which considers either FDI or estimation of one particular air data parameter, this paper focuses on fault-tolerant air data estimation subject to simultaneous angle-of-attack (AOA) and calibrated airspeed (VCAS) sensor faults. This problem involves two main challenges:

- Wind disturbances and latent sensor faults simultaneously affect VCAS measurements. On one hand, the wind estimates are necessary in the FTE to reconstruct AOA and VCAS reliably. On the other hand, the wind estimates also compensate for any undetected fault effect, which makes the generated residual signal much less sensitive to the faults.
- In order to facilitate industrial validation and verification (V&V), the algorithm implementation needs to use an Airbus graphical symbol library called SAO (Specification Assistee par Ordinateur). This library allows automatic code generation for the FCCs used by Airbus, but includes a significantly limited set of mathematical operation blocks [26], [27]. Such a strict constraint limits the complexity level of the implemented algorithm to be compliant with the actual FCCs.

In order to address the above challenges, we propose a fault-tolerant estimator by solving a constrained moving horizon estimation (MHE) problem in real time. This approach exploits a low-order aerodynamics-independent model augmented with first-order integrating wind dynamics. By exploiting constraints, the proposed MHE-based constrained residual generator has improved sensitivity to faults compared to conventional unconstrained residual generators, if some inequality constraints are activated by the faults. Such fault sensitivity improvement is shown by nonlinear programming sensitivity analysis, and can be achieved by any general MHE based FDI incorporating constraints. The implementation challenge of our proposed MHE based FTE method is addressed by adopting a real-time iteration scheme with interior-point (IP) sequential quadratic programming (SQP) strategies. It ensures fixed computational cost per sample by limiting the number of iterations and admitting suboptimal solutions. The real-time feasibility of our algorithm implementation on FCCs has been validated by the industrial V&V.

Compared to our preliminary results in [28], [29], our presented approach in this paper additionally incorporates the ground speed measurements in order to reliably estimate AOA after the total loss of the three redundant AOA sensors. In contrast to the desktop simulations in [28], [29], the results of the industrial validation campaign are presented in this paper to illustrate its real-time feasibility and the promising FDI and estimation performance statistics.

This paper is organized as follows. Section II reviews the objectives, the system model, and challenges in the problem under investigation. Our FTE scheme is proposed in Section III. Then, the advantages of the inequality constraints exploited in FTE are explained in Section IV by comparing with an unconstrained MHE based FTE. Section V discusses the implementation of our proposed method for real-time computation. In section VI, the FDI and estimation performance of our implemented method is assessed in the high-fidelity

nonlinear RECONFIGURE benchmark by intensive simulation runs covering a wide range of the flight envelope.

II. PROBLEM FORMULATION

Civil aircraft are generally equipped with three dedicated sensors for each one of AOA and VCAS measurements. The majority voting scheme is then performed among the three redundant sensors to isolate any faulty sensors and compute a consolidated measurement. Such a triplex redundancy based majority voting scheme works well when only one sensor source is faulty. However, it cannot effectively isolate multiple faulty sources within the triplex redundancy [1]. The objective of this work is to enhance the available hardware redundancy by fault-tolerant estimation, which includes detecting and isolating simultaneous multiple faulty AOA and VCAS sensors, and at the same time, providing reliable estimation of AOA and VCAS. Considering the two main challenges explained in Section I, the proposed FTE method should have fast fault detection, very low rate of false alarms and missed detections, small estimation errors, and allow feasible real-time computational cost for the FCCs.

A. Aerodynamics-independent model subject to winds

The RECONFIGURE project focuses on the longitudinal motion of the aircraft. Thus the following longitudinal model is derived for FTE of AOA and VCAS:

$$\begin{cases} \dot{\alpha}(t) = \mathcal{F}_\alpha(\alpha(t), \Theta(t)) + u_\alpha(t) \\ \dot{V}_g(t) = \mathcal{F}_v(\alpha(t), \Theta(t)) + u_v(t) \\ \dot{\mathbf{w}}(t) = \mathbf{u}_w(t) \\ \mathbf{y}(t) = h(\alpha(t), \mathbf{w}(t), \Theta(t)) \\ \mathbf{y}_m(t) = \mathbf{y}(t) + \mathbf{n}(t) \end{cases} \quad (1)$$

with the definitions $\mathbf{w}(t) = [W_x(t) \ W_z(t)]^T$, $\mathbf{u}_w(t) = [u_{w,x}(t) \ u_{w,z}(t)]^T$, $\mathbf{y}(t) = [V_g(t) \ V_z(t) \ \alpha(t) \ V_c(t)]^T$,

$$\Theta(t) = [V_g(t) \ \theta(t) \ q(t) \ A_x(t) \ A_z(t) \ z(t)]^T, \quad (2)$$

and $\mathbf{n}(t) = [n_{vg}(t) \ n_{vz}(t) \ n_\alpha(t) \ n_{vc}(t)]^T$. The system outputs $\mathbf{y}(t)$ include the ground speed V_g , the vertical speed V_z , the AOA α , and the VCAS V_c . W_x and W_z represent horizontal and vertical wind speeds in the inertial frame, respectively. The model parameter Θ consists of ground speed V_g , pitch angle θ , pitch rate q , horizontal load factor A_x , vertical load factor A_z , and altitude z , which are all measurable. The reason of including V_g , which is one entry of the system outputs, in the model parameter Θ will be explained later in Remark 1. The output equations in (1) for V_z and V_c are

$$V_z = h_{vz}(\alpha, \mathbf{w}, \Theta) \text{ and } V_c = h_{vc}(\alpha, \mathbf{w}, \Theta), \quad (3)$$

respectively. The unknown inputs u_α , u_v , and \mathbf{n} account for the effects of process noises, measurement noises, and the model mismatches. For each redundant AOA sensor measurement $\alpha_m^{(i)}$ or VCAS sensor measurement $V_{c,m}^{(i)}$, $i = 1, 2, 3$, the latent sensor faults $f_\alpha^{(i)}$ and $f_{vc}^{(i)}$ are additive, i.e.,

$$\alpha_m^{(i)} = \alpha + f_\alpha^{(i)} + n_\alpha^{(i)}, \quad V_{c,m}^{(i)} = V_c + f_{vc}^{(i)} + n_{vc}^{(i)}. \quad (4)$$

The first-order integrating model in (1) is a simple yet powerful approximation of the wind dynamics that has been widely used in flight control, e.g., in [30]. $u_{w,x}$ and $u_{w,z}$ represent the unknown horizontal and vertical wind accelerations.

The above system model (1) provides several advantages: (i) it avoids using other air data measurements which are considered as unreliable in the presence of AOA or VCAS sensor faults, and involves only inertial sensors associated with the model parameter Θ and the output \mathbf{y}_m ; (ii) it includes no aerodynamic parameters, thus is independent of aircraft and flight envelope; (iii) it is insensitive to actuator faults and structural damages; (iv) its low state dimensions are attractive for real-time computation.

More details of the aerodynamics-independent longitudinal model (1) are explained in the following. Let $[u \ v \ w]^T$ denote the components of the true airspeed V_t in the body frame, whose relation to V_t is expressed as below with the AOA α and the sideslip angle β :

$$\begin{bmatrix} u \\ v \\ w \end{bmatrix} = \begin{bmatrix} V_t \cos \alpha \cos \beta \\ V_t \sin \beta \\ V_t \sin \alpha \cos \beta \end{bmatrix}.$$

The load factors A_x, A_y, A_z represent the accelerations generated by the aerodynamic forces along the axes of the body frame. The wind speed components in the inertial frame are denoted by $[W_x \ W_y \ W_z]^T$. The roll, pitch, and yaw angles are given by $[\phi \ \theta \ \psi]^T$, respectively, while the roll, pitch, and yaw rates are $[p \ q \ r]^T$ accordingly.

With the above notations, the aircraft dynamics is expressed by [31]

$$\begin{bmatrix} \dot{u} \\ \dot{v} \\ \dot{w} \end{bmatrix} = \begin{bmatrix} A_x \\ A_y \\ A_z \end{bmatrix} + R_{\text{BI}} \begin{bmatrix} 0 \\ 0 \\ g \end{bmatrix} - \begin{bmatrix} p \\ q \\ r \end{bmatrix} \times \begin{bmatrix} u \\ v \\ w \end{bmatrix} - R_{\text{BI}} \begin{bmatrix} \dot{W}_x \\ \dot{W}_y \\ \dot{W}_z \end{bmatrix} \quad (5)$$

where g denotes the gravitational acceleration, and R_{BI} represents the rotational matrix governed by $[\phi \ \theta \ \psi]^T$ to transform a vector in the inertial frame to a vector in the body frame. Since the RECONFIGURE project focuses on the longitudinal motion by assuming negligible lateral motion and constant wind component W_y , we have $v = 0$, $\beta = 0$, $A_y = 0$, $\dot{W}_y = 0$, $\phi = 0$, $\psi = 0$, $p = 0$, and $r = 0$. This results in the simplified longitudinal dynamics

$$\begin{bmatrix} \dot{u} \\ \dot{w} \end{bmatrix} = \begin{bmatrix} A_x \\ A_z \end{bmatrix} + R_{\text{BI}} \begin{bmatrix} 0 \\ g \end{bmatrix} + \begin{bmatrix} -qw \\ qu \end{bmatrix} - R_{\text{BI}} \begin{bmatrix} \dot{W}_x \\ \dot{W}_z \end{bmatrix} \quad (6)$$

derived from (5), with

$$\begin{bmatrix} u \\ w \end{bmatrix} = \begin{bmatrix} V_t \cos \alpha \\ V_t \sin \alpha \end{bmatrix}, \quad R_{\text{BI}} = \begin{bmatrix} \cos \theta & -\sin \theta \\ \sin \theta & \cos \theta \end{bmatrix}. \quad (7)$$

Note that by using the measured load factors A_x and A_z , the dynamic relation (6) becomes independent of aerodynamics, thus is valid for different aircraft with different flight envelopes. Instead of directly using (6) for our problem, we choose to work with the following equivalent model derived from (6) by exploiting (7):

$$\dot{\alpha} = \frac{1}{V_t} f_\alpha(\alpha, \Theta) + q + \frac{1}{V_t} f_{w,\alpha}(\alpha, \mathbf{w}, \Theta), \quad (8)$$

$$\dot{V}_t = f_v(\alpha, \Theta) - f_{w,v}(\alpha, \mathbf{w}, \Theta), \quad (9)$$

with

$$\begin{aligned} f_\alpha(\alpha, \Theta) &= -A_x \sin \alpha + A_z \cos \alpha + g \cos(\alpha - \theta), \\ f_{w,\alpha}(\alpha, \mathbf{w}, \Theta) &= \dot{W}_x \sin(\alpha - \theta) - \dot{W}_z \cos(\alpha - \theta), \\ f_v(\alpha, \Theta) &= A_x \cos \alpha + A_z \sin \alpha + g \sin(\alpha - \theta), \\ f_{w,v}(\alpha, \mathbf{w}, \Theta) &= \dot{W}_x \cos(\alpha - \theta) + \dot{W}_z \sin(\alpha - \theta). \end{aligned}$$

Note that measurements of the true airspeed V_t are unreliable in the presence of VCAS sensor fault [1], thus should not be directly used for the VCAS sensor fault diagnosis. In this case, we replace V_t in (8) with the function

$$\begin{aligned} V_t = h_{vt}(\alpha, \mathbf{w}, \Theta) &= -W_x \cos(\alpha - \theta) - W_z \sin(\alpha - \theta) \\ &+ \sqrt{V_g^2 - [W_x \sin(\alpha - \theta) - W_z \cos(\alpha - \theta)]^2}, \end{aligned} \quad (10)$$

which can be derived from the wind velocity triangle (Equation (1) of [17], Equation (1.5-6) of [32])

$$\begin{cases} V_g^2 = u_g^2 + w_g^2 \\ u_g = u + W_x \cos \theta - W_z \sin \theta \\ w_g = w + W_x \sin \theta + W_z \cos \theta. \end{cases}$$

In order to derive a simplified yet reliable model without involving V_t , we make the following approximations. For the civil aircraft in the RECONFIGURE project [1], we have $V_g \gg |W_x \sin(\alpha - \theta) - W_z \cos(\alpha - \theta)|$, then (10) can be approximated as

$$h_{vt}(\alpha, \mathbf{w}, \Theta) \approx -W_x \cos(\alpha - \theta) - W_z \sin(\alpha - \theta) + V_g. \quad (11)$$

Let $\Delta V = V_t - V_g$ denote the difference between the true airspeed V_t and the ground speed V_g due to the winds. Since we have

$$V_g^2 \gg \Delta V f_\alpha(\alpha, \Theta), V_t \gg f_{w,\alpha}(\alpha, \mathbf{w}, \Theta)$$

for the considered flight scenarios, the approximations

$$\begin{aligned} \frac{1}{V_t} f_\alpha(\alpha, \Theta) &\approx \left(\frac{1}{V_g} - \frac{1}{V_g^2} \Delta V \right) f_\alpha(\alpha, \Theta) \approx \frac{1}{V_g} f_\alpha(\alpha, \Theta), \\ \frac{1}{V_t} f_{w,\alpha}(\alpha, \mathbf{w}, \Theta) &\approx 0 \end{aligned}$$

can be used to derive

$$\dot{\alpha} = \frac{1}{V_g} f_\alpha(\alpha, \Theta) + q + u_\alpha \quad (13)$$

from (8). Similarly, by exploiting (8), (11), and $\dot{\theta} = q$, we are able to approximate (9) with

$$\dot{V}_t = f_v(\alpha, \Theta) + u_v. \quad (14)$$

The above equations (13) and (14) represent the first two equations of the model (1), and u_α and u_v account for the model mismatches including the above unknown approximation errors and the effect of stochastic noises in the measured parameters Θ .

With the airspeed V_t in the body frame and the vertical wind W_z in the inertial frame, the vertical speed measurement $V_{z,m}$ in the inertial frame is expressed by (Equation (2.4-5) of [32])

$$V_{z,m} = -V_t \sin(\alpha - \theta) + W_z + n_{vz}$$

which can be further approximated as

$$V_{z,m} = -V_g \sin(\alpha - \theta) + W_z + n_{vz} \quad (15)$$

due to (11) and $\alpha - \theta \approx 0$.

The output equation for the fault-free VCAS measurement $V_{c,m}$ consists of two conversions: (i) from ground speed V_g to true airspeed V_t via the function $h_{vt}(\alpha, \mathbf{w}, \Theta)$ in (10) and (11); and (ii) from V_t to V_c [33], [34], i.e.,

$$\begin{aligned} V_{c,m} &= \sqrt{5\gamma RT_0 \rho(V_t, T, \bar{p})} + n_{vc}, \\ &= \sqrt{5\gamma RT_0 \rho(h_{vt}(\alpha, \mathbf{w}, \Theta), T, \bar{p})} + n_{vc} \end{aligned} \quad (16)$$

with $T = T_0 + Lz$, $\bar{p} = \left(1 + \frac{L}{T_0}z\right)^{-\frac{g}{RL}}$,

$$\rho(V_t, T, \bar{p}) = \sqrt{\left[\left[\left(1 + \frac{V_t^2}{5\gamma RT}\right)^{3.5} - 1\right]\bar{p} + 1\right]^{\frac{1}{3.5}} - 1},$$

where z , T , and \bar{p} represent pressure altitude, outside air temperature, static pressure scaled by the ground static pressure value, respectively. The constants T_0 , L , R , and γ take their values according to International Standard Atmosphere [33]: $T_0 = 288.15$ K, $L = -6.5$ K/km, $R = 287.05287$ (m/s)²K, and $\gamma = 1.4$. z in Θ , T and \bar{p} in (16) uses altitude measurements. n_{vz} and n_{vc} account for both the unknown approximation errors and the stochastic measurement noises in (15) and (16), respectively.

III. FAULT-TOLERANT MOVING HORIZON ESTIMATION SCHEME

A. Fault-tolerant estimation scheme

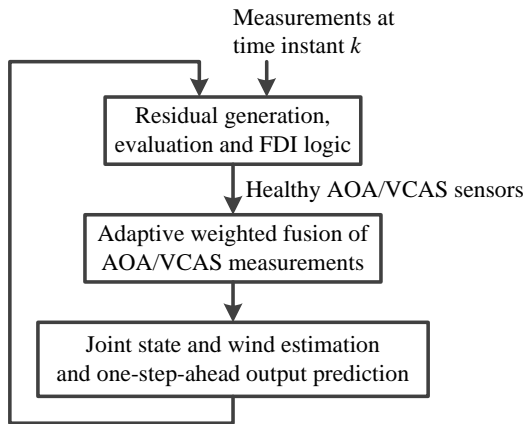


Fig. 1. Fault-tolerant estimation scheme.

As depicted in Fig. 1, our proposed FDI and estimation scheme consists of three consecutive steps:

Step 1. Residual generation, evaluation and FDI logic.

The residual signals for FDI are generated as the difference between the AOA/VCAS measurements $\{\alpha_{m,k}^{(i)}, V_{c,m,k}^{(i)}\}$ and their one-step-ahead predictions $\{\hat{\alpha}_{k|k-1}^{(i)}, \hat{V}_{c,k|k-1}^{(i)}\}$, i.e.,

$$r_{\alpha,k}^{(i)} = \alpha_{m,k}^{(i)} - \hat{\alpha}_{k|k-1}^{(i)}, \quad r_{vc,k}^{(i)} = V_{c,m,k}^{(i)} - \hat{V}_{c,k|k-1}^{(i)}, \quad (17)$$

for $i = 1, 2, 3$. Here, the index k denotes the samples at time instant t_k . The residual signals are evaluated by their root mean square (RMS) values over a sliding window:

$$J_{\star,k}^{(i)} = \sqrt{\frac{1}{N_{\text{eval}}} \sum_{j=k-N_{\text{eval}}+1}^k (r_{\star,j}^{(i)})^2} \quad (18)$$

where \star represents “ α ” and “ vc ”, N_{eval} is the length of residual evaluation window. With a suitable threshold $J_{\star,\text{th}}$, the i th AOA or VCAS sensor is concluded to be faulty if we have $J_{\star,k}^{(i)} > J_{\star,\text{th}}$ for n_D times during the past time window $[k - N_{\text{eval}} + 1, k]$, which allows a confirmation time for the fault detection decision.

Step 2. Adaptive weighted fusion of AOA/VCAS measurements.

Similarly to [20], the redundant AOA sensors identified as fault-free are fused into a weighted mean measurement α_m :

$$\begin{aligned} \alpha_{m,k} &= \sum_{i \in \{J_{\alpha,k}^{(i)} \leq J_{\alpha,\text{th}}\}} \beta_{\alpha,k}^{(i)} \alpha_{m,k}^{(i)}, \\ \beta_{\alpha,k}^{(i)} &= \frac{1}{\sum_{j \in \{J_{\alpha,k}^{(j)} \leq J_{\alpha,\text{th}}\}} \frac{1}{(J_{\alpha,k}^{(j)})^2}} \frac{1}{(J_{\alpha,k}^{(i)})^2}. \end{aligned} \quad (19)$$

The above weights $\beta_{\alpha,k}^{(i)}$ are adaptively computed from the residual RMS values (18), so that the sensors with larger residual RMS values are assigned with lower weights. The same procedure is performed on the VCAS sensors to compute the weights $\beta_{vc,k}^{(i)}$ and the weighted mean value $V_{c,m,k}$. Before a faulty sensor is detected, the undetected faulty sensor is given a lower weight in (19) due to its larger residual RMS value. These adaptively fused measurements are used in the subsequent state and wind estimation, thus the state and wind estimates are less affected by the undetected faults embedded in the lower-weighted sensors.

Step 3. Joint state and wind estimation and one-step-ahead output prediction.

The joint state and wind estimation algorithm computes the filtered estimates $\hat{\alpha}_{k-1|k-1}$ and $\hat{\mathbf{w}}_{k-1|k-1}$ by solving a nonlinear MHE problem that incorporates the bounds of the states and the noisy inputs of the model (1). It then generates the one-step ahead predictions $\hat{\alpha}_{k|k-1}$ and $\hat{V}_{c,k|k-1}$ for the residual generation and evaluation in Step 1 mentioned before.

As will be explained in Section IV, the incorporated constraints in Step 3 effectively improve the fault sensitivity of the generated residual signals.

B. Overview of moving horizon estimation

The MHE technique is well-known for its capability to address nonlinearity, constraints, and robustness to initial errors [35]. It builds on the discrete-time approximation of the continuous-time model (1):

$$\alpha_{k+1} = \alpha_k + t_s \mathcal{F}_\alpha(\alpha_k, \Theta_k) + t_s u_{\alpha,k}, \quad (20a)$$

$$V_{g,k+1} = V_{g,k} + t_s \mathcal{F}_v(\alpha_k, \Theta_k) + t_s u_{v,k}, \quad (20b)$$

$$\mathbf{w}_{k+1} = \mathbf{w}_k + t_s \mathbf{u}_{\mathbf{w},k}, \quad (20c)$$

$$\bar{\mathbf{y}}_{m,k} = h(\alpha_k, \mathbf{w}_k, \Theta_k) + \bar{\mathbf{n}}_k, \quad (20d)$$

where t_s is the sampling interval, (20a)–(20c) are obtained via approximated numerical integration applied to (1). In (20d), the output vector $\bar{\mathbf{y}}_{m,k}$ consists of the ground speed measurement $V_{g,m}$, the vertical speed measurement $V_{z,m}$ and the two fused measurements α_m and $V_{c,m}$ defined in (19). Accordingly, $\bar{\mathbf{n}}_k = [n_{vg,k} \ n_{vz,k} \ n_{\alpha,k} \ n_{vc,k}]^T$ includes the measurement noises, where $n_{\alpha,k}$ and $n_{vc,k}$ are the fused noises

$$n_{\star,k} = \sum_{i \in \{J_{\star,k}^{(i)} \leq J_{\star,\star}\}} \beta_{\star,k}^{(i)} n_{\star,k}^{(i)}, \quad \star \text{ represents } \alpha \text{ or } vc$$

for the fused measurements α_m and $V_{c,m}$ defined in (19). Note that the fault diagnosis decision determines whether or not to include the AOA and VCAS measurements in the output vector $\bar{\mathbf{y}}_{m,k}$. With different configurations of the output vector, the observability property changes, as will be explained in Section III-C.

Given a moving horizon consisting of N samples of output measurements $\{\bar{\mathbf{y}}_{m,l}, \bar{\mathbf{y}}_{m,l+1}, \dots, \bar{\mathbf{y}}_{m,k}\}$ ($l = k - N + 1$) at time instant k , the MHE problem is formulated as

$$\min_{\mathbf{x}_i, \mathbf{u}_i} \frac{1}{2} \left\| \mathbf{x}_l - \mathbf{x}_{l|k}^- \right\|_{\mathbf{P}^{-1}}^2 + \frac{1}{2} \sum_{i=l}^{k-1} \left\| \mathbf{u}_i \right\|_{\mathbf{Q}^{-1}}^2 \quad (21a)$$

$$+ \frac{1}{2} \sum_{i=l}^k \left\| \bar{\mathbf{y}}_{m,i} - h(\mathbf{x}_i, \Theta_i) \right\|_{\mathbf{R}^{-1}}^2$$

$$\text{s.t. } \mathbf{x}_{i+1} = F(\mathbf{x}_i, \mathbf{u}_i, \Theta_i), \quad (21b)$$

$$\mathbf{u}_i^{\text{LB}} \leq \mathbf{u}_i \leq \mathbf{u}_i^{\text{UB}}, \quad i = l, \dots, k-1,$$

$$\mathbf{x}_i^{\text{LB}} \leq \mathbf{x}_i \leq \mathbf{x}_i^{\text{UB}}, \quad i = l, \dots, k,$$

where $\|\mathbf{s}\|_{\mathbf{M}^{-1}}^2$ in (21a) for a vector \mathbf{s} and a positive definite matrix \mathbf{M} represents a weighted vector norm computed as $\mathbf{s}^T \mathbf{M}^{-1} \mathbf{s}$,

$$\mathbf{x} = \begin{bmatrix} \alpha \\ V_g \\ \mathbf{w} \end{bmatrix}, \quad \mathbf{u} = \begin{bmatrix} u_\alpha \\ u_v \\ \mathbf{u}_w \end{bmatrix}, \quad \mathbf{P} = \text{diag}(p_\alpha, p_v, p_w \mathbf{I}_2), \quad (22)$$

$$\mathbf{Q} = \text{diag}(q_\alpha, q_v, q_w \mathbf{I}_2), \quad \mathbf{R} = \text{diag}(R_\alpha, R_{vz}, R_{vc}).$$

The function $F(\cdot)$ in (21b) represents the right-hand sides of (20a)–(20c), and $h(\mathbf{x}_i, \Theta_i)$ is a compact form of $h(\alpha_i, \mathbf{w}_i, \Theta_i)$ defined in (20d). The bounds of the inequality constraints in (21b) can be time-varying to account for different weather or flight conditions. At each time instant k , given the initial condition $\mathbf{x}_{l|k}^-$ and the output sequence $\{\bar{\mathbf{y}}_{m,i}, l \leq i \leq k\}$, the nonlinear programming problem (21) is solved to compute the sequence of state estimates $\hat{\mathbf{x}}_{l|k}, \dots, \hat{\mathbf{x}}_{k|k}$, where the filtered estimate $\hat{\mathbf{x}}_{k|k}$ is used to compute the one-step-ahead AOA and wind predictions. The first term of the objective function (21a) is the so-called arrival cost to account for data before the current estimation horizon. Here, we do not adopt a statistical interpretation of the arrival cost as in [36], which requires heavy computations to update $\mathbf{x}_{l|k}^-$ and \mathbf{P} to represent the information given by the filtered or smoothed density function of \mathbf{x}_l . Instead, similarly to [37], the arrival cost term is updated in a deterministic sense in this paper: we assign $\mathbf{x}_{l|k}^-$ to be the a priori smoothed state estimate $\hat{\mathbf{x}}_{l|k-1}$ obtained by solving (21) over the previous horizon $[l-1, k-1]$, and use \mathbf{P} , \mathbf{Q} , and \mathbf{R}

as tuning parameters to achieve trade-offs between different components of the objective function.

Throughout this paper, the MHE problem (21) with or without inequality constraints is referred to as constrained or unconstrained MHE (CMHE or UMHE), respectively. The benefit of incorporating constraints in residual generation will be analyzed in Section IV by comparing CMHE with UMHE in terms of fault sensitivity. The real-time CMHE implementation will be discussed in Section V.

C. Observability analysis

Let N_α^f and N_v^f represent the number of faulty AOA and VCAS sensors, respectively. As illustrated in Table I, there are four different categories of faulty scenarios, and the output $\bar{\mathbf{y}}_m$ in (20d) needs to be configured accordingly after removing the identified faulty AOA and VCAS sensors:

TABLE I
FOUR CATEGORIES OF FAULT SCENARIOS AND CONFIGURATIONS OF OUTPUTS USED IN THE MHE

Fault category	Number of faulty AOA and VCAS sensors	Configuration of $\bar{\mathbf{y}}_m$ in (20d)
I	$N_\alpha^f < 3, N_v^f < 3$	$[V_{g,m} \ V_{z,m} \ \alpha_m \ V_{c,m}]^T$
II	$N_\alpha^f = 3, N_v^f < 3$	$[V_{g,m} \ V_{z,m} \ V_{c,m}]^T$
III	$N_\alpha^f < 3, N_v^f = 3$	$[V_{g,m} \ V_{z,m} \ \alpha_m]^T$
IV	$N_\alpha^f = 3, N_v^f = 3$	$[V_{g,m} \ V_{z,m}]^T$

Although the proposed method can detect and isolate arbitrary number of AOA and VCAS sensor faults, the reliability of the AOA and VCAS estimates after removing faulty sensors is related to the local observability of the nonlinear discrete-time system (20) under different configurations of $\bar{\mathbf{y}}_m$. For the configuration I in Table I, the matrices of the linearized model ($\mathbf{A}_k, \mathbf{B}_k, \mathbf{C}_k$) of the discrete-time system (20) have the structure

$$\mathbf{A}_k = \begin{bmatrix} a_{11,k} & a_{12,k} & 0 & 0 \\ a_{21,k} & 1 & 0 & 0 \\ 0 & 0 & 1 & 0 \\ 0 & 0 & 0 & 1 \end{bmatrix}, \quad (23)$$

$$\mathbf{C}_k = \begin{bmatrix} 0 & 1 & 0 & 0 \\ c_{21,k} & c_{22,k} & 0 & 1 \\ 1 & 0 & 0 & 0 \\ c_{41,k} & 0 & c_{43,k} & c_{44,k} \end{bmatrix},$$

with the state vector defined in (22).

Remark 1. It is worth noting that the ground speed measurements $V_{g,m}$ are included in the output vector $\bar{\mathbf{y}}_m$ to improve observability of the state α after removing the AOA measurements in the configurations II and III. It is not of primary concern to estimate the state V_g in our problem since we have its fault-free measurement $V_{g,m}$. Because of this reason, we regard V_g as a time-varying measured parameter rather than an unknown state in (11), (15), (16), and (20a), which explains why V_g is included in the model parameter Θ in (2). Therefore, we actually have $a_{12,k} = c_{22,k} = 0$ in (23), which simplifies matrix manipulations in the algorithm implementation explained in Section V-C.

Based on the above linearized model (23), we can make the following observations:

- The states α , V_g , and W_z are locally observable in all the above four configurations of $\bar{\mathbf{y}}_m$ thanks to the availability of the ground speed $V_{g,m}$ and the vertical speed $V_{z,m}$ measurements.
- Due to different numerical ranges of physical variables, the local observability during certain aircraft maneuvers may become weak, which can possibly cause numerical problems in the nonlinear programming based CMHE algorithm. This is especially the case in the configurations II and IV where the AOA is to be estimated after losing AOA measurements. This issue can be alleviated by selecting suitable weighting matrices, in order to improve the numerical conditioning of the QP subproblems in Section V-A.
- The observability of the horizontal wind W_x is attributed only to the availability of VCAS measurements. When we have no VCAS measurements as in the configurations III and IV, W_x becomes neither observable nor detectable (the unobservable W_x cannot be asymptotically reconstructed, see the definition of N -detectability in [38]), and consequently VCAS cannot be reconstructed.

IV. FAULT SENSITIVITY OF MHE-BASED RESIDUAL

In this section, we will analyze the improvement of fault sensitivity by exploiting the inequality constraints in the CMHE based FTE (CMHE-FTE). This is done via nonlinear sensitivity analysis to compare the CMHE-FTE with the UMHE based FTE (UMHE-FTE).

Before a rigorous analysis, some intuitive explanations are first given below. Sensor faults contaminate the measurements before being detected. In the UMHE-FTE, the state and wind estimates compensate for the fault effect when minimizing the objective function (21a), thus the output residuals (17) might be still small even in the presence of faults. In contrast, the CMHE-FTE respects the inequality constraints in (21b). When the presence of faults causes some inequality constraints to become active, the state and wind estimates would be restricted by the active constraints and reluctant to compensate for the fault effect, thus the residuals become more sensitive to faults.

A. Fault Sensitivity of Unconstrained-MHE-based Residual

Let \mathbf{f}_k denote the sensor fault vector included in the measurement $\bar{\mathbf{y}}_{m,k}$. By defining

$$\mathbf{z}_k = [\mathbf{x}_l^T \quad \mathbf{u}_l^T \quad \cdots \quad \mathbf{x}_{k-1}^T \quad \mathbf{u}_{k-1}^T \quad \mathbf{x}_k^T]^T, \quad (24)$$

$$\mathcal{I}_k = \left[(\mathbf{x}_{l|k}^-)^T \quad \mathbf{0}^T \quad \bar{\mathbf{y}}_{m,l}^T \quad \cdots \quad \mathbf{0}^T \quad \bar{\mathbf{y}}_{m,k-1}^T \quad \bar{\mathbf{y}}_{m,k}^T \right]^T, \quad (25)$$

$$\epsilon_k = [\mathbf{0}^T \quad \mathbf{0}^T \quad \mathbf{f}_l^T \quad \cdots \quad \mathbf{0}^T \quad \mathbf{f}_{k-1}^T \quad \mathbf{f}_k^T]^T, \quad (26)$$

$$\mathbf{V} = \text{diag}(\mathbf{P}, \mathbf{Q}, \mathbf{R}, \cdots, \mathbf{Q}, \mathbf{R}, \mathbf{R}),$$

$$F_1(\mathbf{z}_k) = [\mathbf{x}_l^T \quad \mathbf{u}_l^T \quad h^T(\mathbf{x}_l, \Theta_l) \quad \cdots \quad \mathbf{u}_{k-1}^T \quad h^T(\mathbf{x}_{k-1}, \Theta_{k-1}) \quad h^T(\mathbf{x}_k, \Theta_k)]^T,$$

$$F_2(\mathbf{z}_k) = \begin{bmatrix} \mathbf{x}_{l+1} - F(\mathbf{x}_l, \mathbf{u}_l, \Theta_l) \\ \vdots \\ \mathbf{x}_k - F(\mathbf{x}_{k-1}, \mathbf{u}_{k-1}, \Theta_{k-1}) \end{bmatrix},$$

the MHE problem (21) can be compactly written as

$$\hat{\mathbf{z}}_k(\mathcal{I}_k) = \arg \min_{\mathbf{z}_k} \frac{1}{2} \|\mathcal{I}_k - F_1(\mathbf{z}_k)\|_{\mathbf{V}^{-1}}^2 \quad (27)$$

$$\text{s.t. } F_2(\mathbf{z}_k) = \mathbf{0},$$

or equivalently,

$$\hat{\mathbf{z}}_k(\mathcal{I}_k^0, \epsilon_k) = \arg \min_{\mathbf{z}_k} \frac{1}{2} \|\mathcal{I}_k^0 + \epsilon_k - F_1(\mathbf{z}_k)\|_{\mathbf{V}^{-1}}^2 \quad (28)$$

$$\text{s.t. } F_2(\mathbf{z}_k) = \mathbf{0},$$

where the information vector \mathcal{I}_k is decomposed into the nominal part \mathcal{I}_k^0 and the fault perturbation ϵ_k , i.e., $\mathcal{I}_k = \mathcal{I}_k^0 + \epsilon_k$. The inequality constraints in (21b) are omitted in this subsection, and will be discussed in Section IV-B. It can be seen from (27) that the estimate $\hat{\mathbf{z}}_k$ is a function of the information vector \mathcal{I}_k . According to (28), the filtered state estimate can be expressed by $\hat{\mathbf{x}}_{k|k} = \mathbf{P}_s \hat{\mathbf{z}}_k(\mathcal{I}_k^0, \epsilon_k)$, with $\mathbf{P}_s = [\mathbf{0} \quad \cdots \quad \mathbf{0} \quad \mathbf{I}]$. Then, since $\hat{\mathbf{u}}_{k|k} = \mathbf{0}$ is the optimal estimate of \mathbf{u}_k for the MHE problem (21), we construct the one-step-ahead state prediction $\hat{\mathbf{x}}_{k+1|k} = F(\hat{\mathbf{x}}_{k|k}, \hat{\mathbf{u}}_{k|k}, \Theta_k) = F(\hat{\mathbf{x}}_{k|k}, \mathbf{0}, \Theta_k)$ according to (21b), and generate the residual signal as

$$\begin{aligned} \mathbf{r}_{k+1}(\mathcal{I}_{k+1}^0, \epsilon_k, \mathbf{f}_{k+1}) \\ &= \bar{\mathbf{y}}_{m,k+1} - \hat{\mathbf{y}}_{k+1|k} \\ &= \bar{\mathbf{y}}_{m,k+1} - h(\hat{\mathbf{x}}_{k+1|k}, \Theta_{k+1}) \\ &= h(\alpha_{k+1}, \mathbf{w}_{k+1}, \Theta_{k+1}) + \mathbf{f}_{k+1} + \bar{\mathbf{n}}_{k+1} \\ &\quad - h(F(\mathbf{P}_s \hat{\mathbf{z}}_k(\mathcal{I}_k^0, \epsilon_k), \mathbf{0}, \Theta_k), \Theta_{k+1}) \end{aligned} \quad (29)$$

according to the output equation (20d). The sensitivity of the residual signal to faults is characterized by the first-order derivative $\frac{\partial \mathbf{r}_{k+1}}{\partial (\epsilon_k, \mathbf{f}_{k+1})}$.

Remark 2. To analyze disturbance robustness, the output equation (20d) is written into

$$\bar{\mathbf{y}}_{m,k} = h(\alpha_k, \mathbf{0}, \Theta_k) + \mathbf{d}_k + \bar{\mathbf{n}}_k$$

in the fault-free case, with $\mathbf{d}_k = h(\alpha_k, \mathbf{w}_k, \Theta_k) - h(\alpha_k, \mathbf{0}, \Theta_k)$. Then ϵ_k in (26) is redefined as

$$\epsilon_k = [\mathbf{0}^T \quad \mathbf{0}^T \quad \mathbf{d}_l^T \quad \cdots \quad \mathbf{0}^T \quad \mathbf{d}_{k-1}^T \quad \mathbf{d}_k^T]^T$$

to represent the disturbance perturbation in (28) in the fault-free case. By replacing \mathbf{f}_{k+1} in (29) with \mathbf{d}_{k+1} , we obtain the fault-free residual signal $\mathbf{r}_{k+1}(\mathcal{I}_{k+1}^0, \epsilon_k, \mathbf{d}_{k+1})$. Similarly to fault sensitivity, the disturbance robustness of the residual signal in (29) is determined by

$$\frac{\partial \mathbf{r}_{k+1}}{\partial (\epsilon_k, \mathbf{d}_{k+1})} \frac{\partial (\epsilon_k, \mathbf{d}_{k+1})}{\partial (\mathbf{w}_l, \cdots, \mathbf{w}_{k+1})}.$$

Since $\frac{\partial \mathbf{r}_{k+1}}{\partial (\epsilon_k, \mathbf{f}_{k+1})}$ in the faulty case is equal to $\frac{\partial \mathbf{r}_{k+1}}{\partial (\epsilon_k, \mathbf{d}_{k+1})}$ in the fault-free case, higher fault sensitivity generally implies higher sensitivity to disturbances, i.e., lower disturbance robustness.

In order to derive the fault sensitivity of the residual signal in (29), we first derive the fault sensitivity of the estimate $\hat{\mathbf{z}}_k(\mathcal{I}_k^0, \epsilon_k)$, i.e., $\frac{\partial \hat{\mathbf{z}}_k(\mathcal{I}_k^0, \epsilon_k)}{\partial \epsilon_k}$, via sensitivity analysis of the MHE problem (28) parameterized in the fault vector ϵ_k . The Karush-Kuhn-Tucker (KKT) conditions for the optimization problem (28) are given by

$$\begin{aligned} & \mathcal{K}(\mathbf{z}_k, \lambda, \mathcal{I}_k^0, \epsilon_k) \\ &= \begin{bmatrix} -\mathbf{J}_1^T(\mathbf{z}_k) \mathbf{V}^{-1} [\mathcal{I}_k^0 + \epsilon_k - F_1(\mathbf{z}_k)] + \mathbf{J}_2^T(\mathbf{z}_k) \lambda \\ F_2(\mathbf{z}_k) \end{bmatrix} = \mathbf{0} \end{aligned} \quad (30)$$

where we define $\mathbf{J}_1(\mathbf{z}_k) = \frac{\partial F_1(\mathbf{z}_k)}{\partial \mathbf{z}_k}$ and $\mathbf{J}_2(\mathbf{z}_k) = \frac{\partial F_2(\mathbf{z}_k)}{\partial \mathbf{z}_k}$. The solution to the KKT condition (30) is denoted by $\mathbf{z}_k(\mathcal{I}_k^0, \epsilon_k)$ and $\lambda(\mathcal{I}_k^0, \epsilon_k)$ which are implicit functions of \mathcal{I}_k^0 and ϵ_k . The optimal solution associated with the MHE problem (28) is $\hat{\mathbf{z}}_k(\mathcal{I}_k^0, \epsilon_k)$ and $\hat{\lambda}(\mathcal{I}_k^0, \epsilon_k)$. In the neighbourhood of the fault vector ϵ_k , we apply the implicit function theorem to yield

$$\frac{\partial \mathcal{K}(\mathbf{z}_k, \lambda, \mathcal{I}_k^0, \epsilon_k)}{\partial (\mathbf{z}_k, \lambda)} \begin{bmatrix} \frac{\partial \hat{\mathbf{z}}_k}{\partial \epsilon_k} \\ \frac{\partial \hat{\lambda}}{\partial \epsilon_k} \end{bmatrix} + \frac{\partial \mathcal{K}(\mathbf{z}_k, \lambda, \mathcal{I}_k^0, \epsilon_k)}{\partial \epsilon_k} = \mathbf{0}$$

which can be rewritten as

$$\begin{bmatrix} \mathbf{H} & \mathbf{J}_2^T \\ \mathbf{J}_2 & \mathbf{0} \end{bmatrix} \begin{bmatrix} \frac{\partial \hat{\mathbf{z}}_k}{\partial \epsilon_k} \\ \frac{\partial \hat{\lambda}}{\partial \epsilon_k} \end{bmatrix} = \begin{bmatrix} \mathbf{J}_1^T \mathbf{V}^{-1} \\ \mathbf{0} \end{bmatrix}. \quad (31)$$

Note that the Gauss-Newton approximated Hessian $\mathbf{H} = \mathbf{J}_1^T \mathbf{V} \mathbf{J}_1$ is positive definite for the considered MHE problem (21). The dependence of $\hat{\mathbf{z}}_k$ and $\hat{\lambda}$ on \mathcal{I}_k^0 and ϵ_k is omitted hereafter for the sake of brevity. We assume that the linear independence constraint qualification (LICQ) and sufficient-second order condition hold, see Definition 12.4 and Section 12.5 in [39]. Then the invertibility of $\mathbf{J}_2 \mathbf{H}^{-1} \mathbf{J}_2^T$ is ensured, and (31) can be solved by using inversion of block matrices to compute the fault sensitivity of the estimate $\hat{\mathbf{z}}_k$

$$\frac{\partial \hat{\mathbf{z}}_k}{\partial \epsilon_k} = \mathbf{X} \mathbf{J}_1^T \mathbf{V}^{-1} \quad (32)$$

with

$$\mathbf{X} = \mathbf{H}^{-1} - \mathbf{H}^{-1} \mathbf{J}_2^T (\mathbf{J}_2 \mathbf{H}^{-1} \mathbf{J}_2^T)^{-1} \mathbf{J}_2 \mathbf{H}^{-1}. \quad (33)$$

To further derive the fault sensitivity of the residual $\mathbf{r}_{k+1}(\mathcal{I}_{k+1}^0, \epsilon_k, \mathbf{f}_{k+1})$ in (29), we use the notation $\hat{\mathbf{z}}_k(\mathcal{I}_k)$ in (27) instead of $\hat{\mathbf{z}}_k(\mathcal{I}_k^0, \epsilon_k)$ in (28) to express the one-step-ahead output prediction $\hat{\mathbf{y}}_{k+1|k}$ in (29). Define $\hat{\mathcal{I}}_k = F_1(\hat{\mathbf{z}}_k(\mathcal{I}_k))$, then we have $\hat{\mathbf{z}}_k(\mathcal{I}_k) = \hat{\mathbf{z}}_k(\hat{\mathcal{I}}_k)$ according to (28). From (20d) and (21b), the output prediction $\hat{\mathbf{y}}_{k+1|k}$ can be expressed by

$$\begin{aligned} \hat{\mathbf{y}}_{k+1|k} &= h(F(\mathbf{P}_s \hat{\mathbf{z}}_k(\mathcal{I}_k), \mathbf{0}, \Theta_k), \Theta_{k+1}) \\ &= h(F(\mathbf{P}_s \hat{\mathbf{z}}_k(\hat{\mathcal{I}}_k), \mathbf{0}, \Theta_k), \Theta_{k+1}) \\ &= \nu(\hat{\mathcal{I}}_k, \Theta_k, \Theta_{k+1}) \\ &= \nu(F_1(\hat{\mathbf{z}}_k(\mathcal{I}_k)), \Theta_k, \Theta_{k+1}). \end{aligned} \quad (34)$$

In the above equation, the function $\nu(\cdot)$ describes how the output prediction relies on $\hat{\mathcal{I}}_k$, and we define

$$\Phi = \frac{\partial \nu}{\partial \hat{\mathcal{I}}_k}. \quad (35)$$

With $\mathcal{I}_k = \mathcal{I}_k^0 + \epsilon_k$, $\frac{\partial \hat{\mathbf{z}}_k}{\partial \epsilon_k}$ in (32), $\hat{\mathbf{y}}_{k+1|k}$ in (34), and Φ defined in (35), the fault sensitivity of the residual signal (29) can be obtained as

$$\begin{aligned} \mathbf{S}_f &= \frac{\partial \mathbf{r}_{k+1}}{\partial (\epsilon_k, \mathbf{f}_{k+1})} = \begin{bmatrix} \frac{\partial \mathbf{r}_{k+1}}{\partial \epsilon_k} & \frac{\partial \mathbf{r}_{k+1}}{\partial \mathbf{f}_{k+1}} \end{bmatrix} \\ &= \begin{bmatrix} -\frac{\partial \nu}{\partial \hat{\mathcal{I}}_k} \frac{\partial F_1}{\partial \hat{\mathbf{z}}_k} \frac{\partial \hat{\mathbf{z}}_k}{\partial \epsilon_k} & \mathbf{I} \end{bmatrix} = \begin{bmatrix} -\Phi \mathbf{J}_1 \mathbf{X} \mathbf{J}_1^T \mathbf{V}^{-1} & \mathbf{I} \end{bmatrix} \\ &= \begin{bmatrix} \Phi & \mathbf{I} \end{bmatrix} \begin{bmatrix} \mathbf{V} - \mathbf{J}_1 \mathbf{X} \mathbf{J}_1^T & \mathbf{0} \\ \mathbf{0} & \mathbf{I} \end{bmatrix} \begin{bmatrix} \mathbf{V}^{-1} & \mathbf{0} \\ -\Phi & \mathbf{I} \end{bmatrix}. \end{aligned} \quad (36)$$

Different from the fused healthy measurements $\bar{\mathbf{y}}_{m,k}$ used in the MHE problem (21), the original output measurements $\mathbf{y}_{m,k+1}$ in (1) are used in residual generation (29). For the sake of notational simplicity, the complete output vector $\mathbf{y}_{m,k+1}$ is used. If the residual signal of particular sensor(s), e.g., AOA or VCAS, is of interest, then the corresponding rows of \mathbf{r}_{k+1} in the above theorem are selected. In this case, all analysis in Section IV remains the same except that Φ changes according to the selected output components.

B. Fault Sensitivity of Constrained-MHE-based Residual

When the faults are too small to activate any inequality constraints, fault sensitivity of the CMHE-FTE is the same as that of the UMHE-FTE. Next, we will show that the improved fault sensitivity of the CMHE-FTE is attributed to the active inequality constraints caused by sufficiently large faults. In this case, we let $\hat{\mathbf{z}}_k^a$ and \mathbf{r}_{k+1}^a denote the estimate and the residual signal in the presence of the active inequality constraints $F_a(\mathbf{z}_k) \leq \mathbf{0}$. Then the KKT condition (31) becomes

$$\begin{bmatrix} \mathbf{H} & \mathbf{J}_2^T & \mathbf{J}_a^T \\ \mathbf{J}_2 & \mathbf{0} & \mathbf{0} \\ \mathbf{J}_a & \mathbf{0} & \mathbf{0} \end{bmatrix} \begin{bmatrix} \frac{\partial \hat{\mathbf{z}}_k^a}{\partial \epsilon_k} \\ \frac{\partial \hat{\lambda}}{\partial \epsilon_k} \\ \frac{\partial \mu_a}{\partial \epsilon_k} \end{bmatrix} = \begin{bmatrix} \mathbf{J}_1^T \mathbf{V}^{-1} \\ \mathbf{0} \\ \mathbf{0} \end{bmatrix}, \quad (37)$$

where $\mathbf{J}_a^T(\mathbf{z}_k) = \frac{\partial F_a(\mathbf{z}_k)}{\partial \mathbf{z}_k}$, μ_a represents the Lagrange multiplier of the active inequality constraints. Again by applying the inverse of block matrices to (37), we obtain the fault sensitivity of the estimate and the residual signal in the presence of active inequality constraints:

$$\frac{\partial \hat{\mathbf{z}}_k^a}{\partial \epsilon_k} = \mathbf{X}_a \mathbf{J}_1^T \mathbf{V}^{-1}, \quad (38)$$

$$\begin{aligned} \mathbf{S}_f^a &= \frac{\partial \mathbf{r}_{k+1}^a}{\partial (\epsilon_k, \mathbf{f}_{k+1})} \\ &= \begin{bmatrix} \Phi & \mathbf{I} \end{bmatrix} \begin{bmatrix} \mathbf{V} - \mathbf{J}_1 \mathbf{X}_a \mathbf{J}_1^T & \mathbf{0} \\ \mathbf{0} & \mathbf{I} \end{bmatrix} \begin{bmatrix} \mathbf{V}^{-1} & \mathbf{0} \\ -\Phi & \mathbf{I} \end{bmatrix}, \end{aligned} \quad (39)$$

with

$$\mathbf{X}_a = \mathbf{H}^{-1} - \mathbf{H}^{-1} \mathbf{J}_{2a}^T (\mathbf{J}_{2a} \mathbf{H}^{-1} \mathbf{J}_{2a}^T)^{-1} \mathbf{J}_{2a} \mathbf{H}^{-1}, \quad (40)$$

$$\mathbf{J}_{2a} = [\mathbf{J}_2^T \quad \mathbf{J}_a^T]^T, \quad (41)$$

which are in the same form as (32) and (36), respectively.

Given the same fault vector ϵ_{k+1} , the estimate $\hat{\mathbf{z}}_k$ from the UMHE and the estimate $\hat{\mathbf{z}}_k^a$ from the CMHE are the same before the inequality constraints become active. It should be noted that $\hat{\mathbf{z}}_k$ deviates from $\hat{\mathbf{z}}_k^a$ after any inequality constraints in the CMHE remain active due to the presence of faults. In this case, the Jacobian $\mathbf{J}_i(\hat{\mathbf{z}}_k)$ in the UMHE is not equal to

$\mathbf{J}_i(\hat{\mathbf{z}}_k^a)$ in the CMHE, $i = 1$ or 2 , which makes the comparison of the two fault sensitivities not fair. To circumvent this problem, we make the comparison at the same estimate, i.e., $\hat{\mathbf{z}}_k = \hat{\mathbf{z}}_k^a$ at the very first instant that the inequality constraints become active, in the following theorem.

Theorem 1. *Assume that LICQ and sufficient second order condition hold before and after sensor faults occur, and additional inequality constraints become active in the presence of faults. In the neighbourhood of the same estimate $\hat{\mathbf{z}}_k = \hat{\mathbf{z}}_k^a$ from the UMHE and CMHE, we have $\mathbf{S}_f^a(\mathbf{S}_f^a)^T \geq \mathbf{S}_f \mathbf{S}_f^T$, i.e., improved fault sensitivity of the CMHE-FTE compared to the UMHE-FTE. Besides, a larger number of active inequality constraints lead to higher fault sensitivity.*

The proof is given in Appendix A.

V. REAL-TIME MHE ALGORITHM AND ITS IMPLEMENTATION

In this section, we will discuss the implementation of our proposed CMHE based FTE method by using the Airbus SAO library for industrial V&V purposes. For the nonlinear programming problem (21), we adopt the generalized Gauss-Newton (GGN) SQP strategy and use an efficient structure-exploiting IP algorithm to solve each quadratic programming (QP) subproblem. To achieve real-time computation within a short sampling interval, we perform only one SQP iteration per sample and fix the number of iterations in solving each QP subproblem. This real-time iteration strategy, which has been reported in the literature, e.g., in [40], admits sub-optimality of the solution to enable fixed computational cost per sample.

A. Generalized Gauss-Newton SQP

For the current time horizon $[l, k]$, the original problem (21) is first linearized by applying the GGN SQP strategy, around the solution $\hat{\mathbf{x}}_{i|k-1}$ ($i = l, \dots, k$) and $\hat{\mathbf{u}}_{i|k-1}$ ($i = l, \dots, k-1$) over the previous time horizon $[l-1, k-1]$. Note that $\hat{\mathbf{x}}_{k|k-1} = F(\hat{\mathbf{x}}_{k-1|k-1}, \hat{\mathbf{u}}_{k-1|k-1}, \Theta_{k-1})$ is the predicted estimate at time instant $k-1$. This leads to the following QP subproblem:

$$\min_{\Delta \mathbf{x}_i, \Delta \mathbf{u}_i} \frac{1}{2} \|\Delta \mathbf{x}_l\|_{\mathbf{P}^{-1}}^2 + \frac{1}{2} \sum_{i=l}^{k-1} \|\mathbf{r}_{u,i} - \Delta \mathbf{u}_i\|_{\mathbf{Q}^{-1}}^2 \quad (42a)$$

$$+ \frac{1}{2} \sum_{i=l}^k \|\mathbf{r}_{y,i} - \mathbf{C}_i \Delta \mathbf{x}_i\|_{\mathbf{R}^{-1}}^2$$

$$\text{s.t. } \Delta \mathbf{x}_{i+1} = \mathbf{f}_i + \mathbf{A}_i \Delta \mathbf{x}_i + \mathbf{B}_i \Delta \mathbf{u}_i, \quad (42b)$$

$$\Delta \mathbf{u}_i^{\text{LB}} \leq \Delta \mathbf{u}_i \leq \Delta \mathbf{u}_i^{\text{UB}}, \quad i = l, \dots, k-1,$$

$$\Delta \mathbf{x}_i^{\text{LB}} \leq \Delta \mathbf{x}_i \leq \Delta \mathbf{x}_i^{\text{UB}}, \quad i = l, \dots, k,$$

where

$$\mathbf{x}_{l|k}^- = \hat{\mathbf{x}}_{l|k-1}, \quad \Delta \mathbf{x}_i = \mathbf{x}_i - \hat{\mathbf{x}}_{i|k-1}, \quad \Delta \mathbf{u}_i = \mathbf{u}_i - \hat{\mathbf{u}}_{i|k-1},$$

$$\mathbf{r}_{u,i} = -\hat{\mathbf{u}}_{i|k-1}, \quad \mathbf{r}_{y,i} = \bar{\mathbf{y}}_{m,i} - h(\hat{\mathbf{x}}_{i|k-1}, \Theta_i),$$

$$\mathbf{A}_i = \nabla_{\mathbf{x}} F(\hat{\mathbf{x}}_{i|k-1}, \hat{\mathbf{u}}_{i|k-1}, \Theta_i),$$

$$\mathbf{B}_i = \nabla_{\mathbf{u}} F(\hat{\mathbf{x}}_{i|k-1}, \hat{\mathbf{u}}_{i|k-1}, \Theta_i),$$

$$\mathbf{C}_i = \nabla_{\mathbf{x}} h(\hat{\mathbf{x}}_{i|k-1}, \Theta_i),$$

$$\mathbf{f}_i = \hat{\mathbf{x}}_{i|k-1} - \hat{\mathbf{x}}_{i+1|k-1} + t_s F(\hat{\mathbf{x}}_{i|k-1}, \hat{\mathbf{u}}_{i|k-1}, \Theta_i),$$

$$\Delta \mathbf{u}_i^{\text{LB}} = \mathbf{u}_i^{\text{LB}} - \hat{\mathbf{u}}_{i|k-1}, \quad \Delta \mathbf{u}_i^{\text{UB}} = \mathbf{u}_i^{\text{UB}} - \hat{\mathbf{u}}_{i|k-1},$$

$$\Delta \mathbf{x}_i^{\text{LB}} = \mathbf{x}_i^{\text{LB}} - \hat{\mathbf{x}}_{i|k-1}, \quad \Delta \mathbf{x}_i^{\text{UB}} = \mathbf{x}_i^{\text{UB}} - \hat{\mathbf{x}}_{i|k-1}.$$

Its solution $\{\Delta \mathbf{x}_{i|k}, \Delta \mathbf{u}_{i|k}\}$ is computed by using the algorithm given in Section V-B. Finally, the solution to the original problem (21) is updated as $\hat{\mathbf{x}}_{i|k} = \hat{\mathbf{x}}_{i|k-1} + \Delta \mathbf{x}_{i|k}$ and $\hat{\mathbf{u}}_{i|k} = \hat{\mathbf{u}}_{i|k-1} + \Delta \mathbf{u}_{i|k}$, and used to initialize the SQP iteration at the next time instant.

B. Solving the QP subproblem

An infeasible start primal barrier IP method is adopted to solve the QP subproblem (42). We first replace the inequality constraints in the QP (42) with barrier terms in its objective function, to get the approximate problem [39], [41], [42]

$$\min_{\Delta \mathbf{x}_i, \Delta \mathbf{u}_i} \frac{1}{2} \|\Delta \mathbf{x}_l\|_{\mathbf{P}^{-1}}^2 + \frac{1}{2} \sum_{i=l}^{k-1} \|\mathbf{r}_{u,i} - \Delta \mathbf{u}_i\|_{\mathbf{Q}^{-1}}^2 \quad (43)$$

$$+ \frac{1}{2} \sum_{i=l}^k \|\mathbf{r}_{y,i} - \mathbf{C}_i \Delta \mathbf{x}_i\|_{\mathbf{R}^{-1}}^2 + \kappa \phi(\Delta \mathbf{u}, \Delta \mathbf{x})$$

$$\text{s.t. } \Delta \mathbf{x}_{i+1} = \mathbf{f}_i + \mathbf{A}_i \Delta \mathbf{x}_i + \mathbf{B}_i \Delta \mathbf{u}_i, \quad i = l, \dots, k-1$$

where $\kappa > 0$ is a barrier parameter, and the function $\phi(\cdot)$ is the log barrier defined as

$$\begin{aligned} \phi(\Delta \mathbf{u}, \Delta \mathbf{x}) &= \sum_{i=l}^{k-1} \sum_{j=1}^{n_u} \phi_u(\Delta \mathbf{u}_i(j)) + \sum_{i=l}^k \sum_{j=1}^{A_x} \phi_x(\Delta \mathbf{x}_i(j)) \\ \phi_{\star}(\Delta \star_i(j)) &= -\log(\Delta \star_i^{\text{UB}}(j) - \Delta \star_i(j)) \\ &\quad - \log(\Delta \star_i(j) - \Delta \star_i^{\text{LB}}(j)), \end{aligned} \quad (44)$$

with \star representing \mathbf{u} and \mathbf{x} , and j referring to the j th entry of the vector \star . A sequence of the approximate problems (43) are solved iteratively for a decreasing sequence of values of κ , as described in Algorithm 1. For real-time computation, the number of the κ values in the sequence is fixed to n_{κ} , and we perform n_{QP} iterations for each approximate problem (43) with a particular value of κ . A simple backtracking line search is used to ensure that the inequality constraints are satisfied at all iterations.

At each iteration in Algorithm 1, the KKT system of the approximate problem (43) is linearized and solved to compute the search direction represented by $\Delta^2 \mathbf{x}_i$ and $\Delta^2 \mathbf{u}_i$, $i = l, \dots, k$. Such a linearized KKT system is equivalent to the KKT condition of the following linear MHE problem with only equality constraints, omitting detailed explanations for the sake of brevity:

$$\min_{\Delta^2 \mathbf{x}_i, \Delta^2 \mathbf{u}_i} \frac{1}{2} \|\bar{\mathbf{r}}_x - \Delta^2 \mathbf{x}_l\|_{\mathbf{P}^{-1}}^2 + \frac{1}{2} \sum_{i=l}^{k-1} \|\bar{\mathbf{r}}_{u,i} - \Delta^2 \mathbf{u}_i\|_{\mathbf{Q}^{-1}}^2$$

$$+ \frac{1}{2} \sum_{i=l}^k \|\bar{\mathbf{r}}_{y,i} - \bar{\mathbf{C}}_i \Delta^2 \mathbf{x}_i\|_{\mathbf{R}^{-1}}^2$$

$$\text{s.t. } \Delta^2 \mathbf{x}_{i+1} = -\mathbf{r}_{p,i} + \mathbf{A}_i \Delta^2 \mathbf{x}_i + \mathbf{B}_i \Delta^2 \mathbf{u}_i,$$

$$i = l, \dots, k-1. \quad (45)$$

where we define

$$\mathbf{g}_{\star,i} = \text{vect} \left(\left\{ \nabla \phi_{\star}(\Delta \star_i^-(j)) \right\}_{j=1,2,3} \right), \quad (46a)$$

$$\mathbf{L}_{\star,i} = \text{diag} \left(\left\{ \sqrt{\nabla^2 \phi_{\star}(\Delta \star_i^-(j))} \right\}_{j=1,2,3} \right), \quad (46b)$$

with \star being \mathbf{u} and \mathbf{x} ,

$$\mathbf{r}_{p,i} = -\mathbf{f}_i - \mathbf{A}_i \Delta \mathbf{x}_i^- - \mathbf{B}_i \Delta \mathbf{u}_i^- + \Delta \mathbf{x}_{i+1}^-, \quad (46c)$$

$$\bar{\mathbf{r}}_x = -\Delta \mathbf{x}_l^-, \bar{\mathbf{r}}_{u,i} = \mathbf{Q}^{-1} (\mathbf{r}_{u,i} - \Delta \mathbf{u}_i^-) - \kappa \mathbf{g}_{u,i}, \quad (46d)$$

$$\bar{\mathbf{r}}_{y,i} = \begin{bmatrix} \mathbf{r}_{y,i} - \mathbf{C}_i \Delta \mathbf{x}_l^- \\ -\sqrt{\kappa} \mathbf{L}_{x,i}^{-1} \mathbf{g}_{x,i} \end{bmatrix}, \bar{\mathbf{C}}_i = \begin{bmatrix} \mathbf{C}_i \\ \sqrt{\kappa} \mathbf{L}_{x,i} \end{bmatrix}, \quad (46e)$$

$$\bar{\mathbf{R}}_i = \text{diag} (\mathbf{R}_i, \mathbf{I}_{A_x}), \bar{\mathbf{Q}}_i = (\mathbf{Q}^{-1} + \kappa \mathbf{L}_{u,i}^T \mathbf{L}_{u,i})^{-1}. \quad (46f)$$

Note that $\text{vect}(\{x(i)\})$ and $\text{diag}(\{x(i)\})$ in (46a) and (46b) represent a column vector and a diagonal matrix, respectively, with scalar entries $\{x(i)\}$. Because of the above equivalence, the linearized KKT system of (43) is solved by applying a structure-exploiting Riccati based algorithm on the linear UMHE problem (46), which is inspired by Chapter 4 of [42] and detailed in Algorithm 2. In each iteration of Algorithm 1, solving the search direction by Algorithm 2 is the most expensive step whose computational complexity is $O(N(n_x + n_u)^3)$, with n_x and n_u denoting dimensions of the state \mathbf{x}_i and the unknown input \mathbf{u}_i respectively [42].

Algorithm 1 Primal barrier interior-point algorithm

Initialization: $\kappa = \kappa_{\text{init}}, \{\Delta \mathbf{x}_i^- = 0, \Delta \mathbf{u}_i^- = 0\}_{i=l, \dots, k}$.

for $j = 0 \rightarrow n_{\kappa} n_{QP} - 1$ **do**

Linearization: compute all the quantities in (46).

Compute the search direction $\{\Delta^2 \mathbf{x}_i, \Delta^2 \mathbf{u}_i\}_{i=l, \dots, k}$ with Algorithm 2.

Line search:

$$s_j = \max \left\{ 2^{-n_s} \left| \begin{array}{l} \Delta \star_i^{\text{LB}} \leq \eta_{\star,i} (2^{-n_s}) \leq \Delta \star_i^{\text{UB}}, \\ i = l, \dots, k, \text{ and } n_s \leq n_s^{\text{max}} \\ \text{is a nonnegative integer} \end{array} \right. \right\}$$

where $\eta_{\star,i}(\mu) = \Delta \star_i^- + \mu \Delta^2 \star_i$ with \star representing \mathbf{u} and \mathbf{x} . s_j is set to zero if there does not exist a nonnegative integer $n_s < n_s^{\text{max}}$ that satisfies all the inequality constraints.

Update:

$$(\Delta \mathbf{x}_i^-, \Delta \mathbf{u}_i^-) \leftarrow (\Delta \mathbf{x}_i^-, \Delta \mathbf{u}_i^-) + s_j (\Delta^2 \mathbf{x}_i, \Delta^2 \mathbf{u}_i),$$

$\kappa \leftarrow 0.1\kappa$ if j is an integral multiple of n_{κ} .

end for

Solution to the QP (42): $(\Delta \mathbf{x}_{i|k}, \Delta \mathbf{u}_{i|k}) \leftarrow (\Delta \mathbf{x}_i^-, \Delta \mathbf{u}_i^-)$.

C. Implementation aspects

In the RECONFIGURE project, the implementation using SAO is a critical step to assess the feasibility of real-time computation on FCCs. The following aspects have been considered to either speed up computation or simplify the implementation while maintaining good estimation performance.

The overall computational cost is kept small by setting the horizon length N of the MHE problem (21) to be 3. Further increasing the estimation horizon length does not necessarily improve the estimation performance, since more

Algorithm 2 Solve the search direction

1: *Riccati recursion based factorization:*

2: $\hat{\mathbf{P}}_l = \mathbf{P}$

3: **for** $i = l \rightarrow k$ **do**

4: $\Pi_i \leftarrow \bar{\mathbf{C}}_i \hat{\mathbf{P}}_i, \Xi_i \leftarrow (\bar{\mathbf{R}}_i + \Pi_i \bar{\mathbf{C}}_i^T)^{-1}, \Omega_i \leftarrow \bar{\mathbf{C}}_i^T \Xi_i$

5: $\mathbf{K}_i \leftarrow \hat{\mathbf{P}}_i \Omega_i, \mathbf{P}_i^f \leftarrow \hat{\mathbf{P}}_i - \mathbf{K}_i \Pi_i$

6: **if** $i < k$ **then**

7: $\hat{\mathbf{P}}_{i+1} \leftarrow \mathbf{A}_i \mathbf{P}_i^f \mathbf{A}_i^T + \mathbf{B}_i \bar{\mathbf{Q}}_i \mathbf{B}_i^T$

8: **end if**

9: **end for**

10: *Forward recursion:*

11: $\Delta^2 \hat{\mathbf{x}}_l = \bar{\mathbf{r}}_x$

12: **for** $i = l \rightarrow k$ **do**

13: $\check{\mathbf{r}}_i \leftarrow \bar{\mathbf{r}}_{y,i} - \bar{\mathbf{C}}_i \Delta^2 \hat{\mathbf{x}}_i, \Delta^2 \mathbf{x}'_i \leftarrow \Delta^2 \hat{\mathbf{x}}_i + \mathbf{K}_i \check{\mathbf{r}}_i$

14: **if** $i < k$ **then**

15: $\Delta^2 \mathbf{u}'_i \leftarrow \bar{\mathbf{r}}_{u,i}$

16: $\Delta^2 \hat{\mathbf{x}}_{i+1} \leftarrow -\mathbf{r}_{p,i} + \mathbf{A}_i \Delta^2 \mathbf{x}'_i + \mathbf{B}_i \Delta^2 \mathbf{u}'_i$

17: **end if**

18: **end for**

19: *Backward recursion:*

20: $\Delta^2 \mathbf{x}_k \leftarrow \Delta^2 \mathbf{x}'_k, \lambda_{k-1} \leftarrow -\Omega_k \check{\mathbf{r}}_k$

21: **for** $i = k-1 \rightarrow 0$ **do**

22: $\xi_i \leftarrow \mathbf{A}_i^T \lambda_i, \Delta^2 \mathbf{u}_i \leftarrow \Delta^2 \mathbf{u}'_i - \bar{\mathbf{Q}}_i \mathbf{B}_i^T \lambda_i$

23: $\Delta^2 \mathbf{x}_i \leftarrow \Delta^2 \mathbf{x}'_i - \mathbf{P}_i^f \xi_i$

24: **if** $i > 0$ **then**

25: $\lambda_{i-1} \leftarrow \xi_i - \Omega_i (\check{\mathbf{r}}_i + \Pi_i \xi_i)$

26: **end if**

27: **end for**

wind disturbances and measurement noises are included within the horizon. For the purpose of noise filtering in the residual signal, the length N_{eval} of the residual evaluation window in (18) is set to 10, at the cost of slightly increased fault detection delay. The number of iterations n_{κ} and n_{QP} in Algorithm 1 are both fixed to 2, in order to achieve the real-time feasibility on FCCs. Extensive numerical simulations show good results even with such small number of iterations.

As explained in Section III-C, in the configurations (ii)-(iv) of the output vector used in the proposed MHE algorithm, the AOA or VCAS measurements should not be involved when all redundant AOA or VCAS sensors are identified as faulty. However, this cannot be done by directly removing AOA or VCAS from the output equation (20d), because vectors and matrices of time-varying sizes (which are needed to reconfigure the output equation in the MHE algorithm) are not supported in the SAO library. To simplify the SAO implementation for the above issue, we let the output equation (20d) remain the same, but set only the third or fourth row of the matrix \mathbf{C}_i in (42a) to zero after losing all AOA or VCAS sensors, respectively. By doing so, the feedback information from AOA or VCAS becomes ineffective when necessary in one of the configurations (ii)-(iv), and the SAO implementation still works with vectors and matrices of fixed sizes. In particular, this allows the MHE implementation to work on the observable subsystem associated with (α, V_g, W_z) and discard the unobservable W_x in the configurations (iii) and (iv).

Lookup tables are used to approximate logarithm and power computations involved in $g_{x,i}$ and $\mathbf{L}_{*,i}$ in (46) as well as the entries of the fourth row of \mathbf{C}_i .

Computing the search direction by solving the linearized KKT system of (43) dominates the computational cost of Algorithm 1. This step follows Algorithm 2 in the SAO implementation by taking the following strategies:

- The intermediate results, e.g., Π_i , Ξ_i , Ω_i , \mathbf{K}_i in lines 4-5, $\check{\mathbf{r}}_i$ in line 13, and ξ_i in line 22 of Algorithm 2, are reused in subsequent computations.
- The symmetric or diagonal matrix structures are exploited in all the matrix manipulations.
- To compute Ξ_i in line 4 of Algorithm 2, the block matrix inversion formula is applied so that the inversion of the matrix $\bar{\mathbf{R}}_i + \Pi_i \bar{\mathbf{C}}_i^T$ can be reduced to the inversion of several matrices of smaller size which is computed via the analytical adjugate formula.

With all the above efforts, the real-time computational cost of our SAO implementation is 5.8 ms per sample under the industrial assessment performed by Airbus. This highlights the feasibility of applying online optimization based MHE methods on FCCs, although it is still computationally significant from the perspective of an aircraft application.

VI. SIMULATION RESULTS

In this section, the Functional Engineering Simulation environment [1], [27] is used to test the proposed CMHE-FTE approach. We first illustrate its benefits by comparisons with the EKF based FTE (EKF-FTE) and the UMHE-FTE, and then evaluate its effectiveness using multiple parametric runs over a wide range of the flight envelope during different maneuvers.

A. Comparison between the EKF, UMHE, and CMHE based FTE

We compare the proposed CMHE-FTE with conventional unconstrained FTE in terms of robustness to disturbances and sensitivity to faults. In order to illustrate the effect of inequality constraints incorporated in the CMHE-FTE, we use EKF and UMHE in Step 3 of the proposed FTE scheme shown in Fig. 1 for comparisons. As discussed in Section IV-A, the only difference from the CMHE-FTE in the UMHE-FTE lies in the absence of inequality constraints. In the MHE problem (21)-(22), the weighting matrices \mathbf{P} , \mathbf{Q} and \mathbf{R} are determined by the relative belief in the a priori estimate $\mathbf{x}_{l|k}$, the dynamic equation in (21b), and the output equation in (20d), respectively. To be specific, R_α , R_{vz} , and R_{vc} in \mathbf{R} are set to be the measurement noise variances. The weights q_α , q_v , and q_w in \mathbf{Q} are determined by the variances of the lumped disturbances in (21b) caused by winds and model approximation errors. The weight p_α is set to be smaller (or larger) than R_α if there is higher (or lower) belief in the a priori AOA estimates than in the AOA measurements. The same rule applies to the weight p_v with regard to R_{vc} . From the FDI point of view, p_w and q_w have an additional role for a trade-off between fault sensitivity and disturbance robustness, as discussed later in this subsection. The weighting matrices \mathbf{Q} and \mathbf{R} in (21) are used as the covariance matrices in the

EKF, in order to ensure a fair comparison with the UMHE and the CMHE. Other $\mathcal{H}_i/\mathcal{H}_\infty$ fault detection filters [43] are not used in the comparisons because they consider only the FDI performance without providing reliable state estimates. All the simulation runs in this subsection are conducted at a speed of 350 kts and an altitude of 5000 ft.

(i) Robustness to disturbance.

First, we compare the EKF-FTE, UMHE-FTE, and CMHE-FTE in terms of the disturbance robustness. For given wind disturbances, disturbance robustness can be measured by maximum RMS of the residuals for AOA and VCAS, i.e., (18), in the absence of faults: smaller RMS of the residual implies higher robustness to disturbances. We test the above three FTE methods under three wind scenarios shown in Fig. 2. As illustrated in Fig. 3, with the same tuning parameters, the size of the residual signals in each method generally grow with the size of the wind disturbances. Under the wind scenarios 1 and 2, the fault-free residual signals of the EKF-FTE are less robust than the UMHE-FTE and the CMHE-FTE, while the residual signals of the UMHE-FTE and the CMHE-FTE have almost the same size, because no inequality constraints are active in both wind scenarios when solving (21). However, the wind amplitudes in the wind scenario 3 are larger than the assumed bounds of winds in the CMHE-FTE, which activates the inequality constraints in the CMHE-FTE. Therefore the residual signals of the CMHE-FTE become larger than those of the UMHE-FTE in the wind scenario 3. From the results under all three wind scenarios, we can see that the UMHE-FTE and the CMHE-FTE have almost the same robustness to disturbances when the real winds are within their assumed bounds in the CMHE-FTE, while the CMHE-FTE becomes less robust to disturbances than the UMHE-FTE when the real winds are larger than their assumed bounds. This shows that the wind bounds used in the CMHE-FTE need to be properly selected according to the weather and flight conditions.

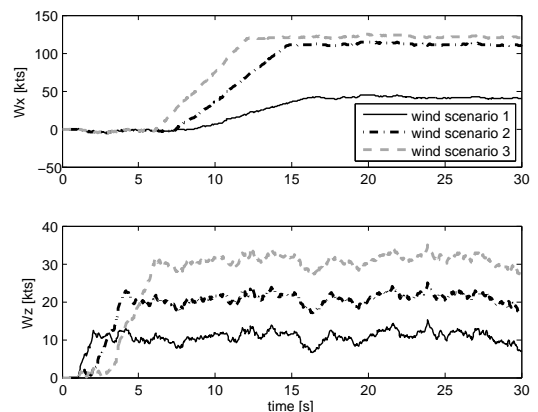


Fig. 2. Three wind scenarios used to compare the EKF, UMHE, and CMHE based FTE.

In the above fault-free simulations, the EKF-FTE gives much larger estimation error than the UMHE-FTE and the CMHE-FTE, and we need larger thresholds to ensure zero false alarms when using the EKF-FTE. Thus under the condition of zero false alarm, the EKF-FTE is less sensitive to

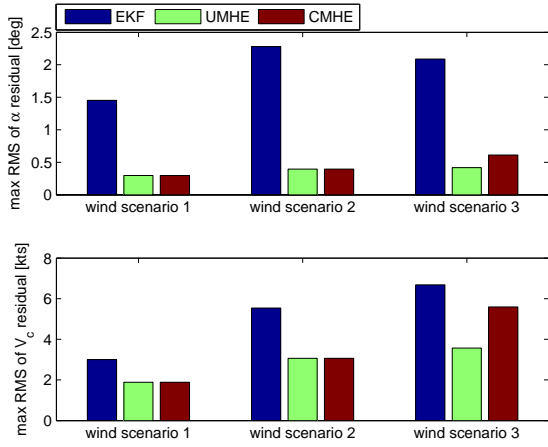


Fig. 3. Comparison of robustness to disturbances of the EKF, UMHE, and CMHE based FTE in different wind scenarios without faults: maximum RMS of the residuals for AOA and VCAS with $p_w = 0.01$ and $q_w = 0.1$.

faults than the UMHE-FTE and the CMHE-FTE with suitably predefined bounds of winds.

(ii) *The benefit of incorporating inequality constraints.*

Next, we illustrate the benefit of incorporating inequality constraints by comparing the UMHE-FTE and the CMHE-FTE in the case of three simultaneous VCAS sensor faults. All AOA sensors are assumed healthy, thus only the detection of VCAS sensor faults is discussed. Both the UMHE-FTE and CMHE-FTE include the AWF strategy, and their detection thresholds are set to be the same. As shown in Fig. 4(c)-(f), the UMHE-FTE compensates for the VCAS sensor faults in its horizontal wind estimate, thus the size of its residual signal fails to trigger the detection threshold. This shows the ineffectiveness of the AWF strategy in the presence of three simultaneous VCAS sensor faults, although it improves fault sensitivity for less than three VCAS sensor faults, as explained in Section III-A. In contrast, as shown in Fig. 4(c), at about 24s, the horizontal wind estimate of the CMHE-FTE reaches its upper bound for the first time, and meanwhile it is still equal to the unconstrained horizontal wind estimate. Fig. 4(d)-(f) further show that at this very time instant, the fault sensitivity of the constrained residuals is significantly higher than that of the unconstrained residuals, which is proved by Theorem 1. After that, the constrained wind estimates still cannot compensate for the fault effects since its upper bound remain active. This leads to the rapid growth of its residual signal with about 4s delay after the fault occurrence. Due to the observability issue explained in Section III-C, the VCAS estimates become unreliable after removing all three faulty VCAS sensors, as in Fig. 4 (b). Similarly to the UMHE-FTE, the EKF-FTE cannot detect all the three faulty VCAS sensors due to the same reason related to the AWF strategy.

We proceed by repeating the test scenario in Fig. 4 with different runaway rates and tuning parameters to highlight the positive effect of inequality constraints on fault sensitivity. Similarly to disturbance robustness, fault sensitivity is not directly evaluated by computing the fault sensitivity matrix S_f^a in (39), because the active constraints required to compute S_f^a

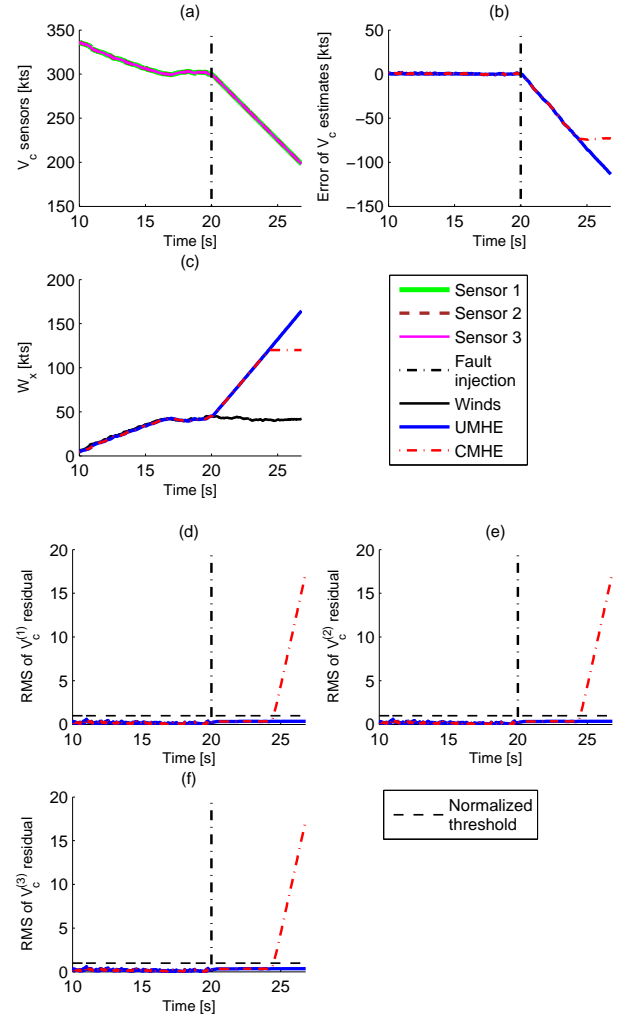


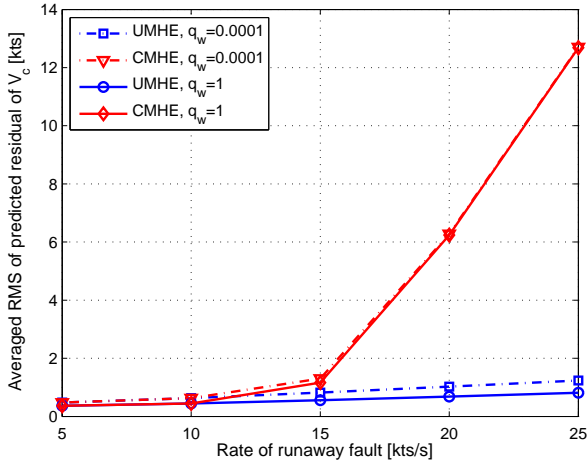
Fig. 4. Comparison of the UMHE-FTE and CMHE-FTE for 3 simultaneous VCAS runaway faults in the wind scenario 1 (runaway rate at -15 kts/s, tuning parameters $p_w = 0.01$ and $q_w = 1$).

are unknown before actually solving the problem (21). Here, we indirectly evaluate fault sensitivity by the averaged RMS of the residual within 17.76s (370 data samples) immediately after fault injection. Larger RMS of the residual implies higher sensitivity to faults.

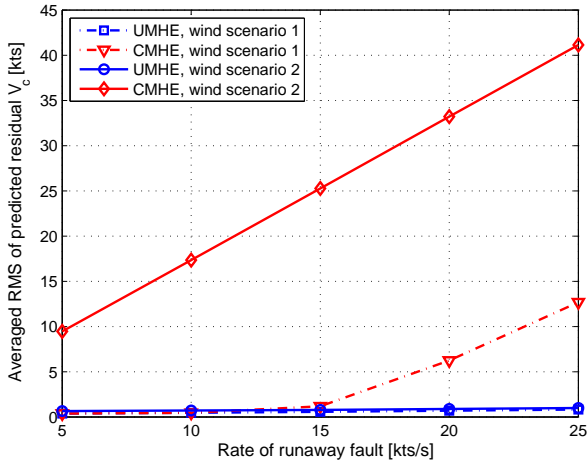
Fig. 5(a) shows the results of the UMHE-FTE and the CMHE-FTE with different tuning parameters q_w and fixed $p_w = 0.01$. The performance comparisons with different p_w are similar, thus omitted. For runaway rate smaller than 10 kts/s, the CMHE-FTE produces approximately the same RMS of the residual as the UMHE-FTE, since the inequality constraints in the CMHE-FTE have become activated for only a very short duration within 17.76s after fault injection. For runaway rate larger than 10 kts/s, the inequality constraints of the CMHE-FTE quickly become active after fault injection. Therefore, the CMHE-FTE gives significantly larger RMS of the residual, which implies higher fault sensitivity, than the UMHE-FTE, given either $q_w = 0.0001$ or $q_w = 1$. Moreover, when q_w increases from 0.0001 to 1, more wind disturbances and a larger portion of fault perturbation can be interpreted

by the assumed wind dynamics in (20c), thus disturbance robustness improves but fault sensitivity decreases. However, it can be seen from Fig. 5(a) that with the same increased q_w , the CMHE-FTE suffers much less from the reduction of fault sensitivity than the UMHE-FTE, especially when the runaway rate is larger than 15 kts/s. The reason is that in the CMHE-FTE the positive effect of active inequality constraints on fault sensitivity compensates for the negative effect of increasing q_w .

To illustrate how the fault sensitivity changes with winds, Fig. 5(b) shows the results of the UMHE-FTE and the CMHE-FTE under two different wind scenarios given in Fig. 2. Even though the wind amplitudes in the wind scenario 2 are significantly larger than in wind scenario 1, the averaged RMS values of the residuals obtained in the UMHE-FTE do not change much in both wind scenarios. However, for the CMHE-FTE, the inequality constraints of the wind estimates are more easily activated in the presence of faults, when the true wind speed or acceleration is already close to the boundary of the inequality constraints. This leads to the significant increase of averaged residual RMS obtained by the CMHE-FTE in the wind scenario 2, compared to that in the wind scenario 1.



(a) Wind scenario 1 in Fig. 2, with $p_w = 0.01$ and different q_w .



(b) Wind scenarios 1 and 2 in Fig. 2, with $p_w = 0.01$ and $q_w = 1$.

Fig. 5. Comparison of sensitivity to faults: RMS of predicted residual signal for different rates of runaway faults.

B. Parametric simulation results

To further evaluate the proposed CMHE-FTE and its real-time implementation, we performed 249 fault-free and faulty parametric runs that sweep grid parameter dispersions over a wide range of the flight envelope during different maneuvers. Diverse wind profiles are simulated, with the amplitudes of wind speeds and accelerations less than 120 kts and 15 kts/s, respectively, in the vertical, longitudinal, and lateral directions. When the lateral motion caused by the lateral wind is not significant, the effect of lateral motion can be regarded as one source of model mismatches in the longitudinal model (1), which is accounted for by the process noise and the measurement noise. Various types of sensor faults are randomly generated and injected into AOA and VCAS sensors, as shown in Table II. Examples of different types of faults can be found in [13], [20]. The duration of each parametric run varies from 60s to 700s. The following metrics are used to evaluate the FDI performance:

- False alarm rate (FAR): percentage ratio of fault-free runs where a fault is incorrectly detected;
- Miss detection rate (MDR): percentage ratio of faulty runs where at least one faulty sensor is not detected;
- False isolation rate (FIR): percentage ratio of faulty runs where at least one healthy sensor is incorrectly identified as faulty;
- Max detection delay (DetD): $\max_i (t_{i,\text{detect}} - t_{i,\text{fault}})$, where $t_{i,\text{detect}}$ and $t_{i,\text{fault}}$ represent the fault detection time and fault occurrence time of the single run indexed by i , respectively;
- Mean detection delay: $\text{mean}_i (t_{i,\text{detect}} - t_{i,\text{fault}})$.

TABLE II
FAULT TYPE, AMPLITUDE, RATE, OR FREQUENCY

Fault type	AOA	VCAS
Oscillation	0.5~25 deg	10~200 kts
Jamming	0.5~1 Hz	0.5~4 Hz
Bias	0.5~25 deg	10~200 kts
Runaway	0.2~25 deg/s	0.5~50 kts/s
Non-return to zero	10% × current value	10% × current value
Noise	Standard deviation	Standard deviation
	1~2 deg	10~20 kts

For the 140 fault-free runs, we get good estimation performance as shown in the first row of Table III. Considering the worst-case estimation errors in the fault-free runs, we set the detection threshold to be $J_{\alpha,\text{th}} = 2.9$ deg and $J_{v_c,\text{th}} = 12$ kts which ensures zero FAR in the fault-free scenarios. The 109 faulty runs can be divided into the four categories listed in Table I, with 47, 22, 25, and 15 runs in each fault category, respectively. We get zero MDR, negligible FIR, and very short detection delay in the overall FDI performance statistics as listed in Table IV. The averaged estimation errors in Table III are also small. Note that the VCAS estimates under the configurations III and IV are not included, because the VCAS cannot be reliably reconstructed in these two configurations due to the unobservability issue explained in Section III-C.

Two representative challenging runs are included here to explain the reasons of the worst-case detection delays and estimation errors in Tables III and IV. In the first representative run, we have a detection delay of 19.16s for the jamming AOA sensors, as shown in Fig. 6(a). It can be seen that the jamming AOA sensor outputs are close to their fault-free values, which keeps the residual RMS values below the given detection threshold. Similar reasons lead to the worst-case detection delays of the VCAS faults in Table IV. The second representative run is under the Configuration III of faulty runs. Although the faults of non-return to zero in all three VCAS sensors are isolated by our proposed approach, the fault information still propagates via the nominal controller without taking any fault-tolerant control strategy, thus leading to fast transients of the fault-free AOA outputs, as in Fig. 6(b). In the presence of such transients, the worst-case absolute estimation error of AOA reaches 16.39 deg, which results in incorrect fault isolation, as shown in Fig. 6(b). This problem can be solved by (i) tuning the threshold and the horizon length of residual evaluation, at the cost of reducing fault detection rate and increasing detection delay; or (ii) reconfigurable control to account for the VCAS sensor faults, which is not within the scope of this paper. Note that the worst-case VCAS estimation errors in Table III are satisfactory compared to the fault-free VCAS measurements in the range from 160 to 360 kts. Dedicated tuning of the weighting matrices, the detection thresholds, and the length of the residual evaluation window can always improve the performance of any particular single run, but it does not necessarily improve the overall performance statistics of multiple runs because of the involved trade-offs among different performance criteria. This suggests that there are potential benefits of adaptive tuning of more algorithm parameters which is left to future research.

TABLE III
ESTIMATION PERFORMANCE OF PARAMETRIC RUNS

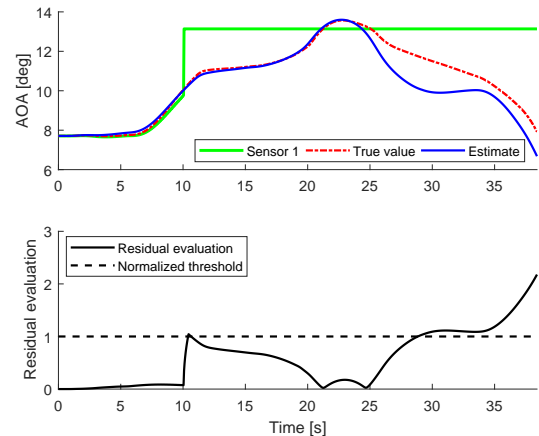
	Max absolute error		Mean absolute error	
	AOA [deg]	VCAS [kts]	AOA [deg]	VCAS [kts]
Fault-free runs	2.44	8.22	0.02	0.02
Faulty runs	16.39	8.22	0.24	0.02

TABLE IV
FAULT DIAGNOSIS PERFORMANCE OF PARAMETRIC RUNS

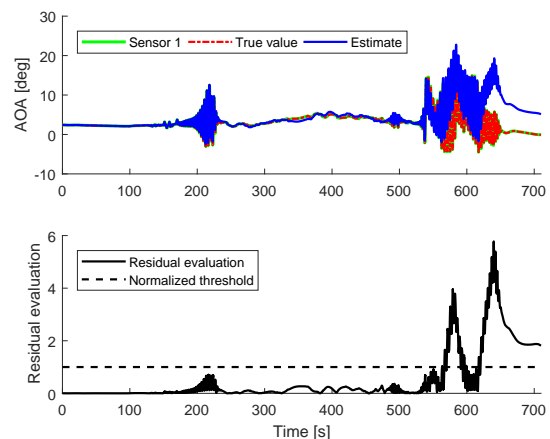
	FAR [%]	MDR [%]	FIR [%]	DetD [s]	
				max	mean
AOA	0	0	0.92	19.16	0.75
VCAS	0	0	0	4.64	0.80

VII. CONCLUSIONS

This paper presented a fault-tolerant moving horizon estimation approach for combined air data sensor fault diagnosis and estimation. Compared to the conventional unconstrained methods, the proposed constrained fault-tolerant estimator improves



(a) Jamming faults in two AOA sensors and two VCAS sensors.



(b) Fault-free AOA sensors and the faults of non-return to zero in three VCAS sensors.

Fig. 6. Results of two representative challenging runs.

the fault sensitivity by incorporating proper wind bounds, without sacrificing robustness to winds. Nonlinear programming sensitivity analysis shows that this benefit applies to general moving horizon estimation based residual generators when imposing state constraints. Using an efficient structure-exploiting algorithm within a real-time iteration scheme, the proposed method was implemented with the Airbus graphical symbol library. Its real-time applicability has been successfully validated in an industrial assessment, and it has achieved satisfactory performance over a wide range of flight envelope when tested in a high-fidelity Airbus simulator. The limitations of using fixed weighting matrices over the entire flight envelope suggest that adaptive tuning of more algorithm parameters is a promising direction to improve the overall diagnosis and estimation performance.

APPENDIX A PROOF OF THEOREM 1

With the same estimate $\hat{\mathbf{z}}_k = \hat{\mathbf{z}}_k^a$, the UMHE and CMHE have the same Ψ , \mathbf{J}_1 , \mathbf{J}_2 , and \mathbf{H} . Let the symmetric matrix Π

denote the matrix square root of the Hessian matrix \mathbf{H} , i.e., $\mathbf{H} = \mathbf{\Pi} \cdot \mathbf{\Pi}$, and define

$$\mathcal{P} = \mathbf{I} - \mathbf{\Pi}^{-1} \mathbf{J}_2^T (\mathbf{J}_2 \mathbf{\Pi}^{-2} \mathbf{J}_2^T)^{-1} \mathbf{J}_2 \mathbf{\Pi}^{-1}, \quad (47)$$

$$\mathcal{P}_a = \mathbf{I} - \mathbf{\Pi}^{-1} \mathbf{J}_{2a}^T (\mathbf{J}_{2a} \mathbf{\Pi}^{-2} \mathbf{J}_{2a}^T)^{-1} \mathbf{J}_{2a} \mathbf{\Pi}^{-1}. \quad (48)$$

Then \mathbf{X} in (33) and \mathbf{X}_a in (40) can be rewritten as

$$\mathbf{X} = \mathbf{\Pi}^{-1} \mathcal{P} \mathbf{\Pi}^{-1} \text{ and } \mathbf{X}_a = \mathbf{\Pi}^{-1} \mathcal{P}_a \mathbf{\Pi}^{-1}, \quad (49)$$

respectively. Let $\mathcal{N}(\cdot)$ denote the left null space of a matrix. It can be seen from (47) and (48) that \mathcal{P} and \mathcal{P}_a are two orthogonal projectors onto the left null spaces $\mathcal{N}(\mathbf{J}_2 \mathbf{\Pi}^{-1})$ and $\mathcal{N}(\mathbf{J}_{2a} \mathbf{\Pi}^{-1})$, respectively (Section 5.13 of [44]). According to (41), the left null space $\mathcal{N}(\mathbf{J}_{2a} \mathbf{\Pi}^{-1})$ is a subset of $\mathcal{N}(\mathbf{J}_2 \mathbf{\Pi}^{-1})$, which implies $\mathcal{P}_a < \mathcal{P}$. Therefore, $\mathbf{X}_a \leq \mathbf{X}$ and $\mathbf{V} - \mathbf{J}_1 \mathbf{X}_a \mathbf{J}_1^T \geq \mathbf{V} - \mathbf{J}_1 \mathbf{X} \mathbf{J}_1^T$ according to (49). Then it can be concluded from (36) and (39) that $\mathbf{S}_f^a (\mathbf{S}_f^a)^T \geq \mathbf{S}_f \mathbf{S}_f^T$.

For the same reason as above, the left null space $\mathcal{N}(\mathbf{J}_{2a} \mathbf{\Pi}^{-1})$ with more active inequality constraints in \mathbf{J}_{2a} is a subset of $\mathcal{N}(\mathbf{J}_2 \mathbf{\Pi}^{-1})$ with fewer active inequality constraints in \mathbf{J}_2 . Hence when more inequality constraints are active in solving the MHE problem, \mathcal{P}_a becomes smaller, and fault sensitivity increases accordingly.

REFERENCES

- [1] P. Goupil, J. Boada-Bauxell, A. Marcos, P. Rosa, M. Kerr, and L. Dalbies, "An overview of the FP7 RECONFIGURE project: industrial, scientific and technological objectives," in *Proceedings of 9th IFAC Symposium on SafeProcess*, Paris, France, 2015, pp. 976–981.
- [2] R. Mehra, C. Rago, and S. Seereeram, "Autonomous failure detection, identification and fault-tolerant estimation with aerospace applications," in *Proceedings of the Aerospace Conference*, Snowmass at Aspen, CO, 1998, pp. 133–138.
- [3] L. H. Mutuel, "Fault-tolerant estimation," Ph.D. dissertation, University of California Los Angeles, 2000.
- [4] I. Rapoport and Y. Oshman, "Efficient fault tolerant estimation using the IMM methodology," *IEEE Transactions on Aerospace and Electronic Systems*, vol. 43, no. 2, p. 492–508, 2007.
- [5] C. Hajiyev and H. E. Soken, "Robust adaptive Kalman filter for estimation of UAV dynamics in the presence of sensor/actuator faults," *Aerospace Science and Technology*, vol. 28, no. 1, pp. 376–383, 2013.
- [6] Y. Gu, J. Gross, M. B. Rhudy, and K. Lassak, "A fault-tolerant multiple sensor fusion approach applied to UAV attitude estimation," *International Journal of Aerospace Engineering*, 2016, doi:10.1155/2016/6217428.
- [7] S. Timotheou, C. G. Panayiotou, and M. M. Polycarpou, "Moving horizon fault-tolerant traffic state estimation for the cell transmission model," in *Proceedings of the 54th IEEE Conference on Decision and Control*, Osaka, Japan, 2015, pp. 3451–3456.
- [8] X. He, Z. Wang, L. Qin, and D. Zhou, "Active fault-tolerant control for an internet-based networked three-tank system," *IEEE Transactions on Control Systems Technology*, vol. 24, no. 6, pp. 2150–2157, 2016.
- [9] X. He, Z. Wang, Y. Liu, L. Qin, and D. Zhou, "Fault-tolerant control for an internet-based three-tank system: Accommodation to sensor bias faults," *IEEE Transactions on Industrial Electronics*, vol. 64, no. 3, pp. 2266–2275, 2017.
- [10] P. Castaldi, W. Geri, M. Bonfè, S. Simani, and M. Benini, "Design of residual generators and adaptive filters for the FDI of aircraft model sensors," *Control Engineering Practice*, vol. 18, no. 5, pp. 449–459, 2010.
- [11] P. Freeman, P. Seiler, and G. Balas, "Air data system fault modeling and detection," *Control Engineering Practice*, vol. 21, pp. 1290–1301, 2013.
- [12] L. Garbarino, G. Zazzaro, N. Genito, G. Fasano, and D. Accardo, "Neural network based architecture for fault detection and isolation in air data systems," in *Proceedings of the 32nd IEEE/AIAA Digital Avionics Systems Conference*, East Syracuse, NY, 2013, pp. 2D4-1 – 2D4-11.
- [13] H. Alwi and C. Edwards, "Development and application of sliding mode LPV fault reconstruction schemes for the ADDSAFE benchmark," *Control Engineering Practice*, vol. 31, pp. 148–170, 2014.
- [14] H. Felemban, J. Che, C. Cao, and I. M. Gregory, "Estimation of airspeed using continuous polynomial adaptive estimator," in *AIAA Guidance, Navigation, and Control Conference*, Maryland, 2014, p. 0267.
- [15] D. Ossmann and H. Joos, "Enhanced detection and isolation of angle of attack sensor faults," in *Proceedings of the AIAA Guidance, Navigation, and Control Conference*, San Diego, California, 2016, doi:10.2514/6.2016-1135.
- [16] M. B. Rhudy, M. L. Fravolini, Y. Gu, M. R. Napolitano, S. Gururajan, and H. Chao, "Aircraft model-independent airspeed estimation without pitot tube measurements," *IEEE Transactions on Aerospace and Electronic Systems*, vol. 51, no. 3, pp. 1980–1995, 2015.
- [17] A. Cho, J. Kim, S. Lee, and C. Kee, "Wind estimation and airspeed calibration using a UAV with a single-antenna GPS receiver and pitot tube," *IEEE Transactions on Aerospace and Electronic Systems*, vol. 47, no. 1, pp. 109–117, 2011.
- [18] S. Hansen and M. Blanke, "Diagnosis of airspeed measurement faults for unmanned aerial vehicles," *IEEE Transactions on Aerospace and Electronic Systems*, vol. 50, no. 1, pp. 224–239, 2014.
- [19] T. Johansen, A. Cristofaro, K. Sorensen, J. Hansen, and T. Fossen, "On estimation of wind velocity, angle-of-attack and sideslip angle of small UAVs using standard sensors," in *Proceedings of 2015 International Conference on Unmanned Aircraft Systems*, Denver, Colorado, 2015, pp. 510–519.
- [20] L. Van Eykeren and Q. P. Chu, "Sensor fault detection and isolation for aircraft control systems by kinematic relations," *Control Engineering Practice*, vol. 31, pp. 200–210, 2014.
- [21] P. Lu, E. van Kampen, C. de Visser, and Q. Chu, "Nonlinear aircraft sensor fault reconstruction in the presence of disturbances validated by real flight data," *Control Engineering Practice*, vol. 49, pp. 112–128, 2016.
- [22] P. Tian, H. Chao, Y. Gu, and S. G. Hagerott, "UAV flight test evaluation of fusion algorithms for estimation of angle of attack and sideslip angle," in *Proceedings of AIAA Guidance, Navigation, and Control Conference*, San Diego, California, 2016, pp. 645–658.
- [23] R. Avram, X. Zhang, J. Campbell, and J. Muse, "IMU sensor fault diagnosis and estimation for quadrotor UAVs," in *Proceedings of the 9th IFAC SafeProcess Conference*, France, 2015, pp. 380–385.
- [24] J. Marzat, H. Piet-Lahanier, F. Damongeot, and E. Walter, "Model-based fault diagnosis for aerospace systems: a survey," *Proceedings of the Institution of Mechanical Engineering, Part G: Journal of Aerospace Engineering*, vol. 226, no. 10, pp. 1329–1360, 2012.
- [25] Q. Shen, B. Jiang, and V. Cocquemot, "Fault diagnosis and estimation for near-space hypersonic vehicle with sensor faults," *Proceedings of the Institution of Mechanical Engineering, Part I: Journal of Systems and Control Engineering*, vol. 226, no. 3, pp. 302–313, 2012.
- [26] D. Briere and P. Traverse, "Airbus A320/A330/A340 electrical flight controls - a family of fault-tolerant systems," in *Proceedings of the 23rd International Symposium on Fault-Tolerant Computing*, Toulouse, France, 1993, pp. 616–623.
- [27] V. Fernández, J. Montañó, C. Recupero, M. Kerr, P. Rosa, J. Boada-Bauxell, and L. Dalbies, "A tool for industrial verification and benchmarking of FDD/FTC designs," in *Proceedings of the 9th IFAC Symposium on SafeProcess*, Paris, France, 2015, pp. 1006–1011.
- [28] Y. Wan, T. Keviczky, and M. Verhaegen, "Robust air data sensor fault diagnosis with enhanced fault sensitivity using moving horizon estimation," in *Proceedings of the 2016 American Control Conference*, Boston, 2016, pp. 5969–5975.
- [29] Y. Wan and T. Keviczky, "Implementation of real-time moving horizon estimation for robust air data sensor fault diagnosis in the RECONFIGURE benchmark," in *Proceedings of the 20th IFAC Symposium on Automatic Control in Aerospace*, Sherbrooke, Quebec, 2016.
- [30] S. S. Mulgund and R. F. Stengel, "Optimal nonlinear estimation for aircraft flight control in wind shear," *Automatica*, vol. 32, no. 1, pp. 3–13, 1996.
- [31] J. W. Langelaan, N. Alley, and J. Neidhoefer, "Wind field estimation for small unmanned aerial vehicles," *Journal of Guidance, Control, and Dynamics*, vol. 2011, no. 4, pp. 1016–1030, 2011.
- [32] B. L. Stevens and F. L. Lewis, *Aircraft Control and Simulation*. John Wiley & Sons, 1992.
- [33] M. Davies, *The Standard Handbook for Aeronautical and Astronautical Engineers*. New York: McGraw-Hill, 2003.
- [34] G. Hardier, C. Seren, P. Ezerzere, and G. Puyou, "Aerodynamic model inversion for virtual sensing of longitudinal flight parameters," in *Proceedings of 2013 Conference on Control and Fault-tolerant Systems*, Nice, France, 2013.
- [35] C. V. Rao, J. B. Rawlings, and D. Q. Mayne, "Constrained state estimation for nonlinear discrete-time systems: stability and moving

- horizon approximations,” *IEEE Transactions on Automatic Control*, vol. 48, no. 2, pp. 246–257, 2003.
- [36] J. B. Rawlings and B. R. Bakshi, “Particle filtering and moving horizon estimation,” *Computers and Chemical Engineering*, vol. 30, no. 10-12, pp. 1529–1541, 2006.
- [37] A. Alessandri, M. Baglietto, and G. Battistelli, “Moving-horizon state estimation for nonlinear discrete-time systems: new stability results and approximation schemes,” *Automatica*, vol. 44, pp. 1753–1765, 2008.
- [38] D. Sui and T. A. Johansen, “Moving horizon observer with regularisation for detectable systems without persistence of excitation,” *International Journal of Control*, vol. 84, no. 6, pp. 1041–1054, 2011.
- [39] J. Nocedal and S. J. Wright, *Numerical Optimization*, 2nd ed. New York, USA: Springer, 2006.
- [40] P. Kuhl, M. Diehl, T. Kraus, J. P. Schlöder, and H. G. Bock, “A real-time algorithm for moving horizon state and parameter estimation,” *Computers and Chemical Engineering*, vol. 35, pp. 71–83, 2011.
- [41] B. M. Bell, J. V. Burke, and G. Pillonetto, “An inequality constrained nonlinear kalman-bucy smoother by interior point likelihood maximization,” *Automatica*, vol. 45, pp. 25–33, 2009.
- [42] N. Haverbeke, “Efficient numerical methods for moving horizon estimation,” PhD Thesis, Katholieke Universiteit Leuven, 2011.
- [43] S. X. Ding, *Model-Based Fault Diagnosis Techniques: Design Schemes, Algorithms and Tools*, 2nd ed. Springer-Verlag London, 2013.
- [44] C. D. Meyer, *Matrix Analysis and Applied Linear Algebra*. SIAM Press, 2000.